Materials Advances

ROYAL SOCIETY OF CHEMISTRY

PAPER

View Article Online
View Journal | View Issue

Cite this: *Mater. Adv.*, 2026, 7, 913

Sustainable TiO_2 photocatalysts modified with hollyhock-derived carbon dots and natural dye for enhanced visible-light degradation of Congo red: a comparative study

Govar H. Hamasalih,[a] Sewara J. Mohammed *[b] and Shujahadeen B. Aziz *[c]

This study introduces a sustainable method for valorizing *Alcea rosea* (hollyhock) floral waste by developing two novel TiO_2-based photocatalysts modified with biomass-derived materials: a natural dye (HH dye) and carbon dots (HHCDs). The HHCDs were synthesized *via* a one-pot hydrothermal process at 180 °C, yielding oxygen-rich, amorphous carbon dots. TiO_2 nanoparticles were prepared by a sol–gel method and subsequently modified with either HH dye or HHCDs through environmentally benign procedures. Comprehensive characterization (FTIR, XRD, UV-vis, and FE-SEM) confirmed the successful incorporation of both modifiers and their interaction with the TiO_2 surface. Optical analysis indicated a significant reduction in the bandgap for both composites, with HH dye@TiO_2 (~2.67 eV) exhibiting a lower bandgap than HHCDs@TiO_2 (~2.89 eV). Electrochemical measurements revealed that HHCDs@TiO_2 facilitated more effective charge carrier separation, whereas HH dye@TiO_2 demonstrated superior light-harvesting capabilities due to its anthocyanin content. In photocatalytic degradation experiments under visible light, HHCDs@TiO_2 demonstrated superior performance, achieving 97.1% degradation of Congo red dye within 80 minutes, compared to 96.8% in 120 minutes for HH dye@TiO_2. Both composites exhibited remarkable long-term stability, retaining over 95% of their efficiency after 180 days of storage. Optimal degradation conditions were identified at mildly acidic to neutral pH using 0.04 g of HHCDs@TiO_2 and 0.06 g of HH dye@TiO_2. This work presents a novel, dual-approach strategy for fabricating efficient and eco-friendly photocatalysts, highlighting their significant potential for solar-driven water purification and environmental remediation.

Received 9th September 2025,
Accepted 20th November 2025

DOI: 10.1039/d5ma01037c

rsc.li/materials-advances

1. Introduction

The extensive use of synthetic dyes in industries such as textiles, paper, and plastics has led to the discharge of large volumes of dye-contaminated wastewater, posing significant threats to aquatic ecosystems and public health.[1] Among these pollutants, azo dyes such as Congo red (CR) are particularly concerning due to their complex aromatic structure, high solubility, and resistance to natural biodegradation, coupled with their potential carcinogenic properties.[2,3] The intense color of CR can significantly impede photosynthesis by reducing light penetration in aquatic ecosystems.[4] Moreover, CR may degrade into benzidine, a known carcinogen, leading to long-term ecological and biological harm.[5,6] These adverse characteristics establish CR as a critical model pollutant for evaluating advanced wastewater treatment technologies.[7]

Conventional treatment methods, including adsorption, coagulation, and flocculation, are often ineffective, as they primarily transfer contaminants between phases rather than degrading them.[8] In contrast, advanced oxidation processes (AOPs), particularly heterogeneous photocatalysis, offer a more sustainable approach by utilizing light energy to generate reactive oxygen species (ROS), which mineralize organic pollutants into harmless end products.[9,10] Titanium dioxide (TiO_2) has been widely used as a photocatalyst due to its non-toxicity, low cost, and chemical stability. However, its practical application is hampered by two primary limitations: a wide bandgap (~3.2 eV for anatase and ~3.0 eV for rutile), which restricts its photoactivity to the ultraviolet region (only ~4% of the solar spectrum), and the rapid recombination of photogenerated electron–hole pairs, which drastically reduces quantum efficiency.[11–13]

[a] *Department of Physics, College of Education, University of Sulaimani, Old Campus, Kurdistan Regional Government, Sulaymaniyah 46001, Iraq*
[b] *Department of Chemistry, College of Science, University of Sulaimani, Qlyasan Street, Kurdistan Regional Government, Sulaymaniyah 46001, Iraq. E-mail: sewara.mohammed@univsul.edu.iq*
[c] *Turning Trash to Treasure Laboratory (TTTL), Research and Development Center, University of Sulaimani, Qlyasan Street, Kurdistan Regional Government, Sulaymaniyah 46001, Iraq. E-mail: shujahadeenaziz@gmail.com*

To overcome these limitations, TiO_2 has been modified through various strategies, including metal/non-metal doping, coupling with narrow-bandgap semiconductors, and sensitization with organic dyes or carbon-based nanomaterials.[14,15] Among these, natural dyes and carbon dots (CDs) derived from plant biomass have emerged as promising, green, and cost-effective modifiers for enhancing the visible-light response of TiO_2.[16,17] Natural dyes, rich in anthocyanins and flavonoids, are abundant, biodegradable, and exhibit excellent light-harvesting capabilities in the visible spectrum.[18,19] Hollyhock (*Alcea rosea*), an ornamental plant, produces vividly pigmented flowers that are typically discarded after blooming. This floral waste represents a valuable and untapped source of natural dyes with inherent electron-donating and photosensitizing properties suitable for photocatalysis.[20]

Carbon dots, a class of zero-dimensional, carbon-based nanomaterials, have also gained significant attention ascribed to their tunable photoluminescence, high surface area, biocompatibility, and ability to facilitate electron transfer.[21–24] CDs can improve charge separation, broaden light absorption, and contribute to up-conversion luminescence.[25,26] When derived from plant-based dyes, they offer a dual advantage, converting biomass waste into functional nanomaterials while enhancing photocatalyst performance. Nevertheless, scalable, low-cost methods for preparing CD-based photocatalysts remain a challenge, limiting their widespread application.[27,28]

Compared to synthetic modifiers, which often involve complex, energy-intensive processes and potentially toxic precursors, biomass-derived materials offer a compelling green alternative. Their advantages include abundance, biodegradability, low cost, and inherent surface functional groups that enhance pollutant adsorption and facilitate semiconductor anchoring. While challenges in scalability and precise control of properties persist, the valorization of agricultural waste into functional photocatalytic materials represents a significant stride towards a circular economy.[29–31] Recent research has demonstrated the potential of biomass-derived CDs as eco-friendly photocatalyst modifiers.[32] However, few studies have directly compared the performance of TiO_2 modified with natural dyes and their corresponding CDs derived from the same biomass source. Such comparisons are essential for understanding structure–activity relationships and optimizing green photocatalyst design for practical and industrial use.

This study demonstrates a sustainable approach by synthesizing and comparatively evaluating two TiO_2-based photocatalysts modified with hollyhock-derived natural dye (HH dye) and hollyhock-derived carbon dots (HHCDs), both sourced from the same floral waste. The photocatalysts were thoroughly characterized to understand their structural, morphological, optical, and electrochemical properties. Their performance was evaluated through the degradation of Congo red under visible light irradiation. This work not only contributes to the development of efficient, waste-derived photocatalysts for water purification but also provides fundamental insights into the distinct mechanistic roles of a natural dye and its corresponding carbon dots in enhancing TiO_2 photocatalysis. The findings align with the principles of waste valorization and support broader efforts towards achieving the United Nations Sustainable Development Goals (SDGs) for clean water and sustainable production.

2. Experimental section

2.1 Materials

Hollyhock flowers (*Alcea rosea*), used for extracting natural dye (HH dye) and synthesizing hollyhock dye-derived carbon dots (HHCDs), were collected from the garden of the University of Sulaimani's Research and Development Center (Sulaymaniyah, Kurdistan Region, Iraq). Titanium(IV) isopropoxide ($Ti[OC(CH_3)_2]_4$ (TTIP), $\geq$97%, Sigma-Aldrich) served as the titanium precursor. Ethanol (C_2H_5OH, 99.9%), hydrochloric acid (HCl, 37%, Merck), and deionized (DI) water were used for sol–gel synthesis. Congo red (CR, $C_{32}H_{22}N_6Na_2O_6S_2$, 99.5%, Merck) was employed as the model pollutant. All chemicals were used as received without further purification.

2.2 Instrumentations

Fourier transform infrared (FT-IR) spectroscopy (V_{max} in cm^{-1}) with KBr pellet methodon a PerkinElmer spectrophotometer (Waltham, MA, USA) was used to find the characteristic functional groups. The ^1H and ^{13}C nuclear magnetic resonance (NMR) spectra were obtained using a 600 MHz Bruker BioSpin spectrometer (Rheinstetten, Germany) using DMSO-d_6 as the solvent. Photocatalytic degradation was monitored by recording UV-visible absorption spectra using a UV 6100 double beam spectrophotometer with a wavelength range of 190–1100 nm, while diffuse reflectance spectra (DRS) were collected on a Varian Cary 100 UV-Vis spectrophotometer equipped with a DRA-CA-30I integrating sphere to determine the optical band gap. X-ray diffraction (XRD) was performed using an Angstrom Advance ADX 2700 diffractometer (Massachusetts, USA) under Cu Kα radiation (λ = 1.5406 Å), which scanned the 10–80° 2θ range with a step size of 0.1°. Photoluminescence (PL) spectra were measured with a Cary Eclipse fluorescence spectrophotometer (Agilent Technologies, USA). HRTEM was carried out using an FEI Tecnai G2 F30. At the same time, the surface chemical composition and elemental states were analyzed using X-ray photoelectron spectroscopy (XPS) with a Thermo Fisher ESCALAB 250Xi instrument. Morphological features were examined by field-emission scanning electron microscopy (FE-SEM) coupled with energy-dispersive X-ray spectroscopy (EDS) using a TESCAN MIRA3 system (Czechia) and photoreactor 2 $\times$ 30 W flood blue light LED lamps.

2.3 Methodologies

2.3.1 Extraction of the HH dye. The extraction of natural colorants often involves time- and energy-intensive processes. To address these challenges, ultrasound-assisted extraction (UAE) was employed as an efficient alternative to conventional methods, offering advantages such as reduced extraction time, lower energy consumption, and improved pigment yield.[33] Fresh hollyhock (HH) flowers were collected, air-dried in the

shade to preserve light-sensitive phytochemicals (*e.g.*, anthocyanins),[34] and ground into a fine powder using brief pulsed blending to avoid heat generation. For the extraction, 8 g of powdered hollyhock was suspended in 200 mL of ethanol, chosen for its efficacy in disrupting plant cell walls and solubilizing polar pigments while minimizing thermal degradation.[35]

The suspension was subjected to sonication using a UIP500hdT ultrasonic processor (20 kHz, 250 W), with the probe immersed directly in the solution. During the 10-minute sonication, the temperature naturally increased from 20 °C to 65 °C due to cavitation effects. After allowing it to settle for 10 minutes, the extract was decanted. The residual plant material was then re-extracted twice using 150 mL of ethanol under identical sonication conditions to maximize pigment recovery.

The combined extracts were purified by sequential filtration through Whatman No. 40 filter paper to remove coarse particulates, followed by 0.22 μm syringe filtration to remove finer debris. The filtrate was concentrated using a rotary evaporator, and the resulting dye was further dried in a silica gel desiccator. The final dry yield of the HH dye was 2.25 g (~28.1%), which was stored at 4 °C for subsequent characterization and application, as shown in Scheme 1a.

2.3.2 Synthesis of HHCDs from the HH dye. HHCDs were synthesized from the HH dye *via* a hydrothermal method. Briefly, 0.5 g of HH dye was dissolved in 100 mL of ethanol and transferred to a Teflon-lined stainless-steel autoclave. The

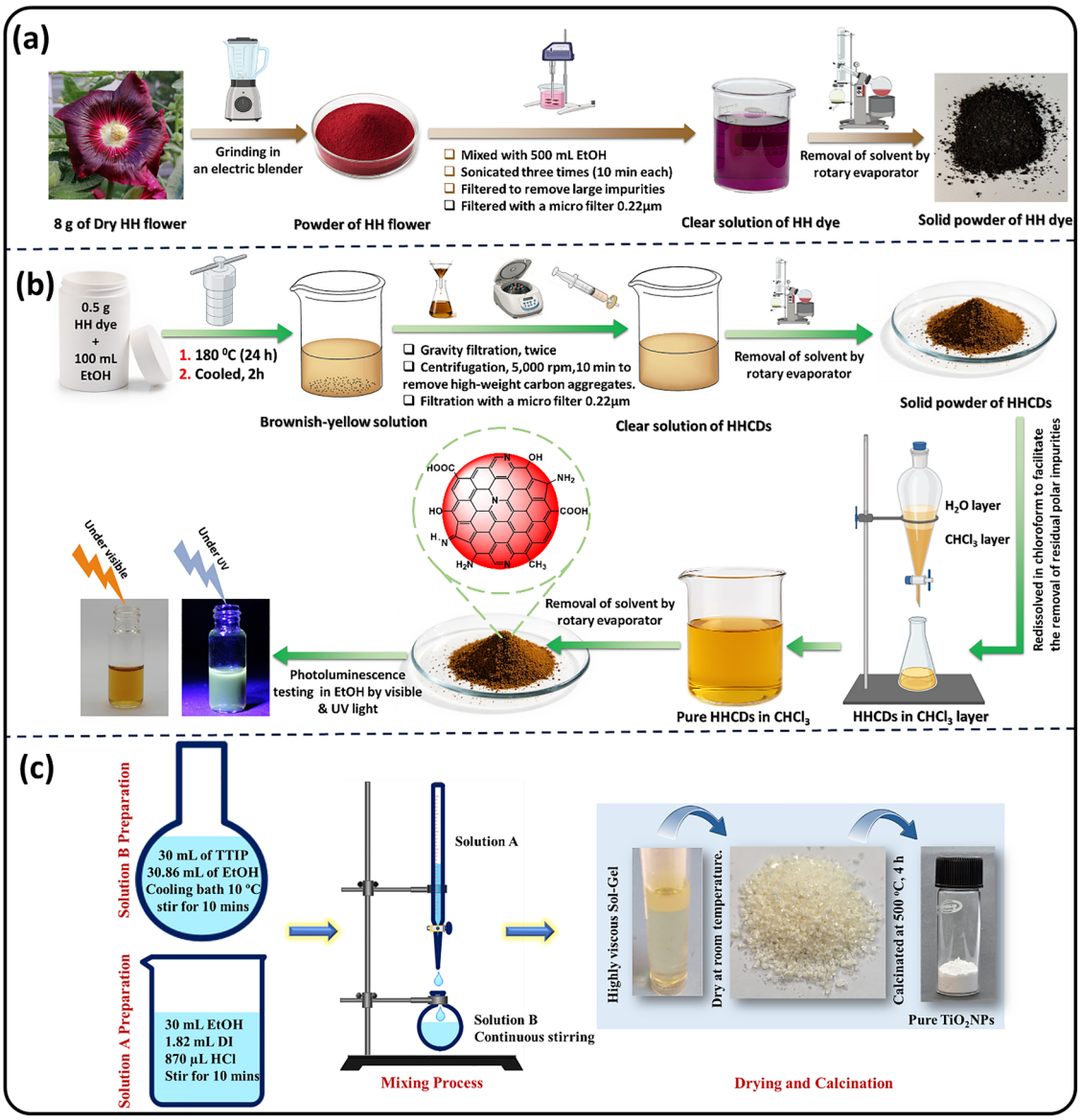

Scheme 1 (a) The stepwise extraction process of the HH dye, (b) the hydrothermal synthesis procedure of the HHCDs from the HH dye, and (c) the sol–gel synthesis process of pure TiO_2 nanoparticles, including hydrolysis, condensation, gelation, drying, and calcination steps.

mixture was heated at 180 °C for 24 h under hydrothermal conditions and then allowed to cool to room temperature, yielding a brownish-yellow solution.

The solution was filtered twice through Whatman No. 40 filter paper (Whatman International Ltd, Kent, UK) to remove coarse particulates and then centrifuged at 5000 rpm for 10 min to separate larger carbonaceous aggregates. The supernatant was further purified by filtration through a 0.22 μm PTFE syringe filter. The solvent was evaporated under reduced pressure using a rotary evaporator, and the residue was redissolved in chloroform to facilitate the removal of residual polar impurities.

Liquid–liquid extraction was performed three times using a chloroform/water (1 : 1 v/v) system. The chloroform phase was collected and concentrated under reduced pressure, yielding 0.5 g (50% yield) of purified brownish-yellow HHCDs. The final product was stored at 4 °C for subsequent characterization and photocatalytic studies (Scheme 1b illustrates the synthesis procedure of the HHCDs).

2.3.3 Synthesis of TiO_2 nanoparticles *via* a sol–gel method. The TiO_2 nanoparticles (TiO_2NPs) were synthesized using a sol–gel method with titanium(IV) isopropoxide (TTIP) as the precursor, following a modified reported procedure.[18] The synthesis involved preparing two separate solutions with a molar ratio of TTIP : DI water : EtOH : HCl = 1 : 1 : 10 : 0.1.

Solution A was prepared by mixing 30 mL of ethanol with 1.82 mL of deionized water and 870 μL of HCl, followed by stirring for 10 min. Solution B was prepared by combining 30 mL of TTIP with 30.86 mL of ethanol in a round-bottom flask, maintained at 10 °C using a cooling bath, and stirred continuously.

Solution A was added dropwise to solution B at a rate of 1 drop every 5 s under stirring at 10 °C, resulting in a transparent solution. Stirring was continued for an additional 10 min, after which the mixture was aged for 24 h to form a thick gel. The gel was transferred to a glass Petri dish and dried at room temperature for 48 h, yielding pale yellow TiO_2 materials. These were ground into a fine powder using a mortar and pestle, then calcined at 500 °C for 4 h in a muffle furnace to obtain white TiO_2NPs, as illustrated in Scheme 1c.

2.3.4 Fabrication of HH dye@TiO_2 and HHCDs@TiO_2 nanocomposites. The nanocomposites of HH dye@TiO_2 and HHCDs@TiO_2 were prepared *via* a solution dispersion method. In the optimized procedure, 0.3 g of HH dye and 0.3 g of HHCDs were separately mixed with 3 g of TiO_2 nanoparticles (weight ratio 0.1 : 1) in 150 mL of ethanol. The mixtures were stirred at 25 °C in the dark for 30 minutes, during which the color of TiO_2 changed from white to dark blue in the dye-doped system (HH dye@TiO_2) and became brown in the CD-doped system (HHCDs@TiO_2), confirming successful composite formation (Scheme 2a and b).

The resulting precipitates were washed 3–4 times with distilled water to remove unbound dye or carbon dots, then dried overnight at 50 °C in an oven. The final composites were stored in amber vials to prevent photodegradation before characterization and photocatalytic testing.

2.3.5 Photodegradation of Congo red using HH dye@TiO_2 and HHCDs@TiO_2 under visible light. The photocatalytic performance of the HH dye@TiO_2 and HHCDs@TiO_2 composites was evaluated for the visible-light degradation of the CR dye. Experiments were conducted in a glass test tube (25 × 150 mm) serving as the photocatalytic reactor, illuminated by two 30 W blue LED floodlights positioned behind the reactor to ensure

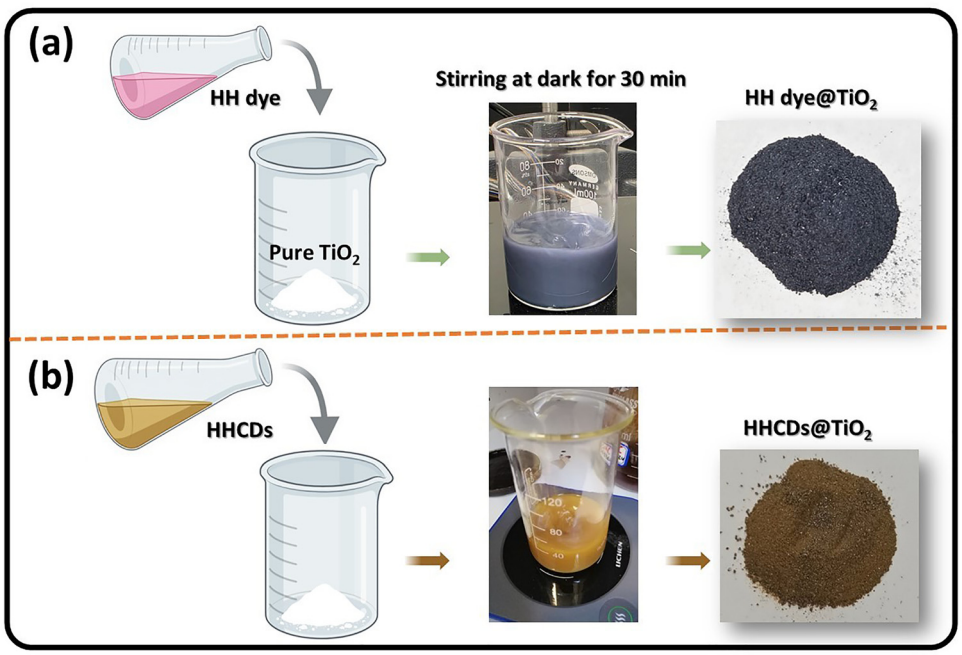

Scheme 2 Illustration of the fabrication process and the photographs of the resulting (a) HH dye@TiO_2 and (b) HHCDs@TiO_2 nanocomposites.

uniform light distribution without significant heating. The setup was enclosed in an aluminum foil-lined box to prevent external light interference. A 30 W blue LED source with an optical output of approximately 7.5 W was used for visible-light irradiation, providing an estimated power density of 18.75 mW cm^{-2} over an illuminated area of 400 cm^2, as confirmed with a calibrated lux meter.

Before irradiation, 0.02–0.07 g of photocatalyst was dispersed in 50 mL of CR solution (10 ppm) and stirred in the dark for 30 min to achieve adsorption–desorption equilibrium. The mixture was then exposed to visible light under constant stirring, with an electric fan maintaining the temperature at 25 °C. At intervals of 30, 60, 90, and 120 min, 5 mL aliquots were withdrawn, centrifuged to remove the catalyst, and analyzed by UV-vis spectrophotometry at λ_{max} = 497 nm to monitor CR degradation. The recovered photocatalysts were washed with distilled water, dried at 60 °C, and reused for recyclability studies.

The effects of irradiation time (30–120 min), catalyst dosage (0.02–0.07 g), initial dye concentration (5–20 ppm), and solution pH (4.17, 5.75, and 8.70) were systematically investigated. Unless otherwise specified, a fixed irradiation time of 60 min was applied for all experiments except those assessing time-dependent degradation or recyclability. Photocatalyst stability was evaluated over five consecutive cycles, with washing and drying between runs to ensure reproducibility.

The degradation efficiency (%) was calculated as:

$$\text{Degradation (\%)} = \frac{C_0 - C_t}{C_0} \times 100\% \quad (1)$$

where C_0 and C_t are the initial and time-dependent CR concentrations (mg L^{-1}), respectively.[36]

2.3.6 Quantum yield (QY) determination. The quantum yield (Φ) of the photocatalysts was determined using fluorescein as the reference standard.[37] Φ was calculated from the relative absorbance (A), integrated fluorescence emission intensity (I), and refractive index (η) of the samples compared to the reference according to:

$$\Phi = \Phi_R \frac{I}{I_R} \frac{A_R}{A} \frac{\eta^2}{\eta_R{}^2} \quad (2)$$

where subscript R denotes the reference (fluorescein) and unsubscripted terms correspond to the tested photocatalysts.

3. Results and discussion

3.1 HH dye characterization

The FTIR spectrum of the HH dye (Fig. 1a) reveals the presence of various functional group characteristics of polyphenolic and flavonoid-rich plant extracts.[38,39] A broad absorption band at 3366 cm^{-1} corresponds to O–H and N–H stretching vibrations, indicating the presence of hydroxyl and amine groups typically found in natural pigments such as anthocyanins,[40] while the peaks at 2924 cm^{-1} and 2851 cm^{-1} are attributed to aliphatic C–H stretching.[41,42] A strong band at 1716 cm^{-1} is assigned to C=O stretching (carbonyl groups), likely from anthocyanins or other conjugated systems, and the band at 1638 cm^{-1} corresponds to aromatic C=C stretching vibrations.[43] Additional

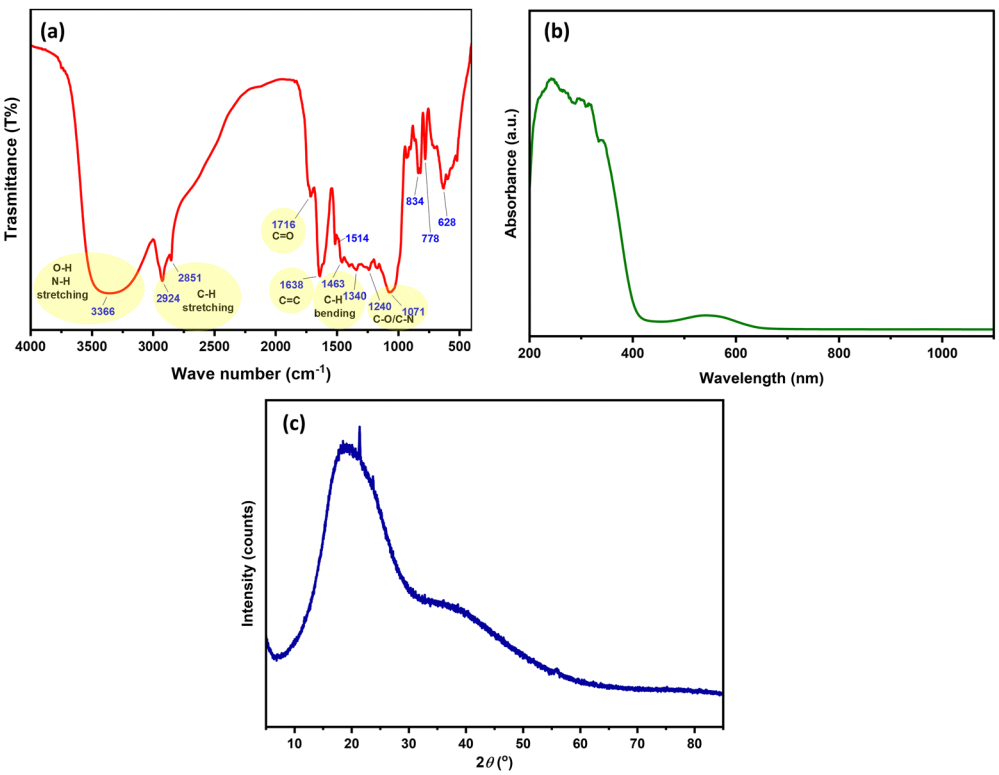

Fig. 1 (a) FTIR spectrum, (b) UV-vis absorption spectrum, and (c) XRD pattern of the HH dye.

peaks at 1463 cm^{-1} and 1340 cm^{-1} are associated with C–H bending of aliphatic carbons.[44] Absorptions between 1240 and 1071 cm^{-1} correspond to C–O and C–N stretching, indicating the presence of ether and amine functionalities.[45–47] These functional groups suggest strong potential for interfacial interactions with TiO_2 surfaces.

The UV-vis absorbance spectrum of the HH dye (Fig. 1b) exhibits strong absorption in the UV and visible regions, with a distinct band at ~550 nm, attributed to an n–π* electron transition.[48] This suggests its efficient visible-light harvesting capability, which is crucial for enhancing the photocatalytic activity of TiO_2 under visible light. Dyes are enriched with colorants and anthocyanins, and thus their absorption will cover the UV to visible region of electromagnetic radiation.

The XRD analysis, as shown in (Fig. 1c), confirms the amorphous nature of the HH dye. This is evidenced by a broad diffraction band centered within the 2θ range of approximately 16° to 24°, characteristic of amorphous structural features.[49]

3.2 Structural and morphological characterization of HHCDs

The HHCDs were synthesized *via* an eco-friendly hydrothermal method using the HH dye as a dual carbon and nitrogen source. The synthesized HHCDs were characterized using multiple techniques, including FTIR, ^{1}H-NMR, ^{13}C-NMR, XPS, UV-vis spectroscopy, photoluminescence (PL), HR-TEM, and XRD. These techniques were employed to elucidate the chemical structure, optical properties, and morphology of the HHCDs, clarifying their role in improving the visible-light photocatalytic activity of sustainable TiO_2 systems.

3.2.1 FTIR spectrum analysis of HHCDs. The FTIR spectrum of HHCDs derived from the HH dye (Fig. 2a) exhibits distinct shifts, indicating chemical transformation during carbonization. A broad band at 3390 cm^{-1} is attributed to O–H stretching from surface hydroxyl and carboxyl groups, which enhances hydrophilicity.[50] The aliphatic C–H stretching bands remain visible at 2921 cm^{-1} and 2851 cm^{-1}. A prominent peak at 1715 cm^{-1} confirms the presence of carboxylic C═O functionalities.[51] Notably, the band at 1655 cm^{-1} is assigned to C═N stretching, suggesting nitrogen incorporation, possibly in the form of an imine or pyridinic structure.[52] Graphitic C═C vibrations appear around 1624 cm^{-1} and 1608 cm^{-1}, indicating retention of conjugated systems.[53,54] A C–H bending peak is observed at 1371 cm^{-1}. Peaks at 1241 cm^{-1} and 1173 cm^{-1} correspond to C–O and C–N bonds, which contribute to surface polarity and potential interaction with TiO_2.[55,56]

Collectively, these results verify that the carbonization process not only preserves but also enhances key functional groups on the HHCDs, including hydroxyl, carbonyl, and nitrogen-containing species. These groups are critical for promoting interfacial charge transfer and boosting photocatalytic activity. The incorporation of CDs with such a rich functional group landscape is crucial for improving the light–matter interactions of TiO_2, thereby enhancing its overall photocatalytic performance. Further insights into the role of CDs within the TiO_2 composite structure are discussed in the subsequent sections.

3.2.2 ^{1}H-NMR spectrum analysis of HHCDs. The ^{1}H-NMR spectrum of HHCDs in DMSO-d_6 (Fig. 2b) reveals diverse proton environments, reflecting their structural complexity.

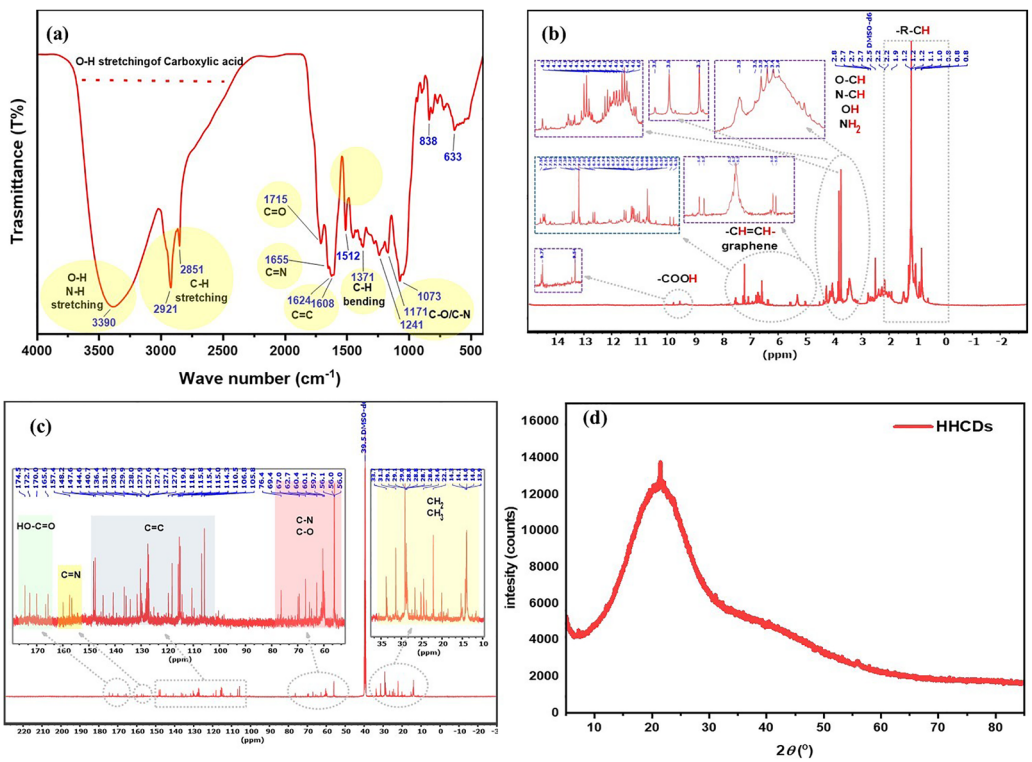

Fig. 2 (a) FT-IR spectrum, (b) ^{1}H-NMR spectrum (DMSO-d_6), (c) ^{13}C-NMR spectrum (DMSO-d_6), and (d) XRD pattern of HHCDs.

Broad signals in the 9.77–9.54 ppm region are assigned to acidic protons (–COOH or –OH), confirming the presence of surface carboxyl/phenolic groups,[57] which enhance aqueous stability and facilitate electron transfer in photocatalysis. Multiple peaks between 7.56 and 5.02 ppm arise from aromatic protons (–CH═CH–), indicating a graphitic carbon framework and retained sp^2-hybridized structures derived from the HH dye precursor.[58] The 4.3–3.4 ppm region shows protons adjacent to electronegative atoms (O–CH, N–CH, –OH, $–NH_2$), further supporting nitrogen and oxygen incorporation, and suggesting increased polarity and potential electron-donating capabilities.[58] Finally, signals at 2.8–0.8 ppm correspond to aliphatic protons ($–CH_3$, $–CH_2–$), reflecting residual hydrocarbon chains that contribute to the amphiphilic nature and dispersibility of HHCDs in aqueous systems.[59,60]

3.2.3 ^{13}C-NMR spectrum analysis of HHCDs. The ^{13}C-NMR spectrum of HHCDs in DMSO-d_6 (Fig. 2c) provides detailed insights into their carbon framework and functionalization. Distinct signals in the 174–165 ppm region are assigned to carboxyl carbons (–COOH), confirming the presence of oxidized surface groups critical for water solubility and photocatalytic activity.[59] The appearance of peaks between 159 and 156 ppm corresponds to aromatic carbons adjacent to nitrogen (C═N), verifying the presence of nitrogen elements, a key feature for enhancing electron density and surface reactivity.[61] The regions belonging to 148–105 ppm reveal the prominent sp^2-hybridized carbon (C═C) signals, indicating a graphitic core that facilitates light absorption and charge transfer.[62] Furthermore, the peaks between 76 and 56 ppm are attributed to C–O and C–N bonds, suggesting hydroxyl and amine functional groups, which improve aqueous stability and HHCD interactions.[63] Finally, signals at 13–33 ppm arise from aliphatic carbons ($–CH_3$, $–CH_2–$), likely from residual hydrocarbon chains during synthesis.[63] These ^{13}C-NMR results are in excellent agreement with the FTIR and ^{1}H-NMR findings, confirming the presence of diverse surface functionalities, including carboxyl, hydroxyl, amine, and aromatic moieties, which collectively enhance the photocatalytic performance of the HHCD-modified TiO_2 system.

3.2.4 XRD analysis of HHCDs. The crystalline structure of the synthesized HHCDs was examined using X-ray diffraction (XRD). As shown in Fig. 2d, the XRD pattern exhibits a broad diffraction peak centered at $2\theta \approx 22.75^\circ$, which corresponds to the (002) plane of disordered graphitic carbon.[64] The peak's broadness and low intensity signify a lack of long-range crystalline order, confirming the predominantly amorphous nature of the HHCDs.[65] This structural characteristic is typical for carbon dots synthesized *via* green, bottom-up routes and is known to profoundly influence their optical and electronic properties, including charge carrier mobility and light absorption. The observed pattern is consistent with previous reports on biomass-derived carbon dots, thereby validating the successful formation of HHCDs through the presented sustainable synthesis method.

3.2.5 X-ray photoelectron spectroscopy (XPS) analysis of HHCDs. XPS analysis provided comprehensive insights into the surface composition and chemical bonding states of the HHCDs. The survey spectrum (Fig. 3a) exhibits three prominent peaks at binding energies of 284.96 eV (C 1s), 400.03 eV (N 1s), and 522.79 eV (O 1s), confirming the co-existence of carbon, nitrogen, and oxygen as primary surface elements.[66,67] The relative intensities of these peaks indicate successful nitrogen incorporation during the carbonization process, a crucial feature for modifying the electronic structure of the carbon dots. The high-resolution C 1s spectrum (Fig. 3b) reveals the complex chemical environment of carbon atoms, with deconvoluted peaks at 283.9 eV (C–C sp^3 hybridized carbon),[68] 284.5 eV (C═C/C–C graphitic carbon),[69] 285.4 eV (C–OH hydroxyl groups),[70] 286.17 eV (C–O/C–N ether/amine linkages),[71] and 287.4 eV (C═O carbonyl groups).[72] This distribution confirms the presence of both aromatic domains and oxygenated functional groups, consistent with our FTIR and NMR results. The N 1s spectrum (Fig. 3c) further demonstrates nitrogen incorporation through three characteristic components at 398.7 eV (pyridinic N, C═N), 399.4 eV (pyrrolic N, N–H), and 401.1 eV (graphitic N, C–N), which are known to enhance charge carrier density and surface reactivity.[73,74]

Complementary information comes from the O 1s spectrum (Fig. 3d), where deconvolution yields four components at 531.2 eV (C═O carbonyl), 532.0 eV (C–O epoxy/ether), 532.8 eV (C–OH/C–O–C hydroxyl/ester), and 533.3 eV (adsorbed water/oxygen species).[75–77] The predominance of oxygen-containing functional groups explains the excellent aqueous dispersibility of HHCDs observed during synthesis and application. These XPS findings collectively demonstrate that HHCDs possess an ideal surface chemistry for photocatalytic applications, combining conjugated sp^2 carbon domains for charge transport, nitrogen dopants for enhanced electron density, and oxygen functional groups for improved interfacial interactions with TiO_2.

3.2.6 HR-TEM analysis of HHCDs. The HR-TEM analysis revealed the morphological and structural characteristics of the HHCDs. Fig. 4a–c show that the HHCDs possess a uniform spherical morphology with narrow size distribution (Fig. 4d), demonstrating excellent synthetic control. This spherical geometry maximizes the surface-to-volume ratio while ensuring optimal dispersibility, crucial for photocatalytic applications.

High-magnification HR-TEM images (Fig. 4c) reveal well-defined lattice fringes with an interplanar spacing of 0.208 nm. This measurement corresponds to the (100) crystallographic plane of graphitic carbon and aligns well with the value of 0.21 nm reported by Guo *et al.*[78] This observation confirms the presence of sp^2-hybridized carbon domains within the HHCD structure, indicating a partially ordered graphitic framework embedded in an amorphous carbon matrix.[79] This structure is further corroborated by the selected-area electron diffraction (SAED) pattern (Fig. 4c inset), which displays characteristic diffuse rings.

This unique nanoarchitecture is pivotal to the optoelectronic properties of the HHCDs.[80,81] The embedded graphitic domains facilitate efficient charge carrier transport *via* π–π* electronic transitions, while the surrounding amorphous

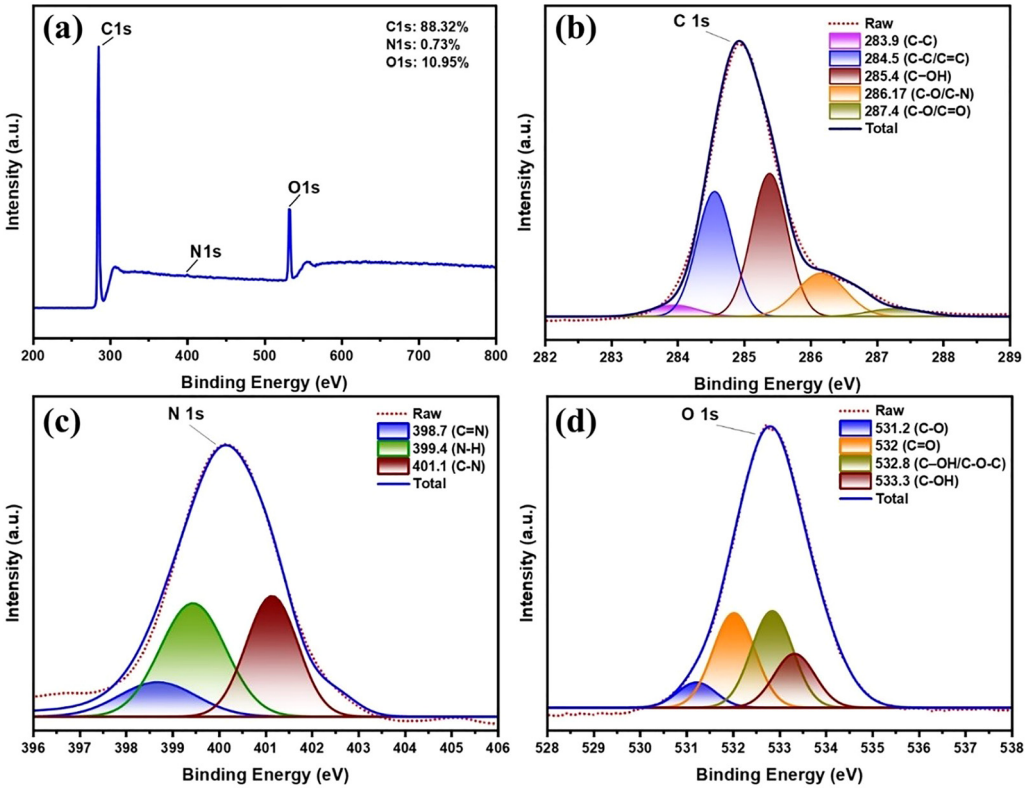

Fig. 3 XPS analysis of HHCDs: (a) full survey spectrum showing elemental composition, (b) high-resolution C 1s spectrum with chemical state deconvolution, (c) N 1s spectrum revealing nitrogen bonding configurations, and (d) O 1s spectrum detailing oxygen functional groups.

regions host abundant surface functional groups that enhance photoluminescence and allow for facile surface modification.

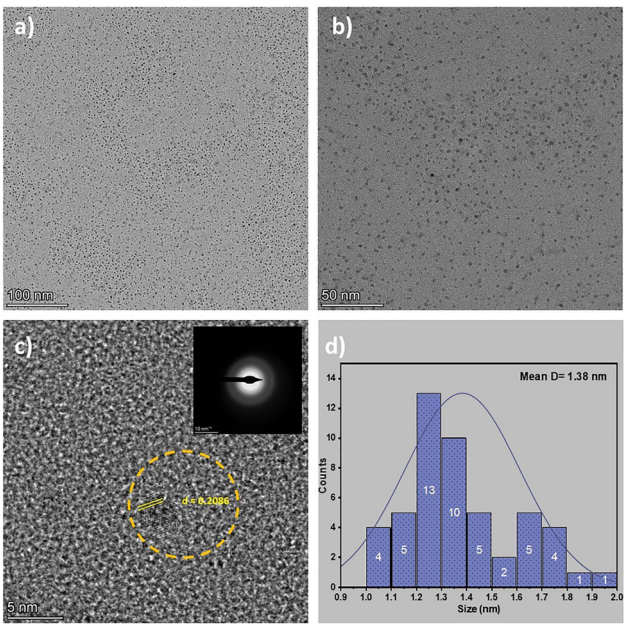

Fig. 4 (a)–(c) HR-TEM images at progressively higher magnifications (scale bars: 100, 50, and 5 nm, respectively) showing spherical morphology, with an inset in (c) displaying the SAED pattern; (d) particle size distribution histogram demonstrating narrow size dispersion.

Furthermore, the narrow particle size distribution of 5–10 nm (Fig. 4d) is optimal for enhancing visible-light absorption and promoting charge separation. These structural attributes are highly advantageous for photocatalysis. They facilitate improved interfacial electron transfer within the HHCD–TiO_2 composite, ultimately leading to the enhanced degradation of Congo red dye under visible light irradiation.

3.2.7 PL spectroscopy analysis of HHCDs. The optical properties of HHCDs were systematically investigated using UV-visible absorption and photoluminescence (PL) spectroscopy in ethanol solution. As shown in Fig. 5a, the UV-vis absorption spectrum displays a prominent band at 410 nm, attributed to n–π* transitions of carbonyl and amine functional groups on the HHCD surface.[82] This electronic transition is the characteristic of carbon dots with nitrogen-containing surface moieties. The HHCD solution appears pale yellow under visible light but exhibits intense cyan emission when irradiated with 365 nm UV light (Fig. 5a inset), demonstrating their strong fluorescence properties.

PL analysis revealed excitation-dependent emission behavior, as evidenced by the series of emission spectra collected from 310 to 450 nm excitation (Fig. 5b). The maximum emission intensity occurs at 490 nm when excited at 410 nm, which corresponds to the absorption maximum observed in the UV-vis spectrum. This excitation–emission relationship was further confirmed by the excitation spectrum monitored at 490 nm (Fig. 5a), verifying 410 nm as the optimal excitation wavelength.

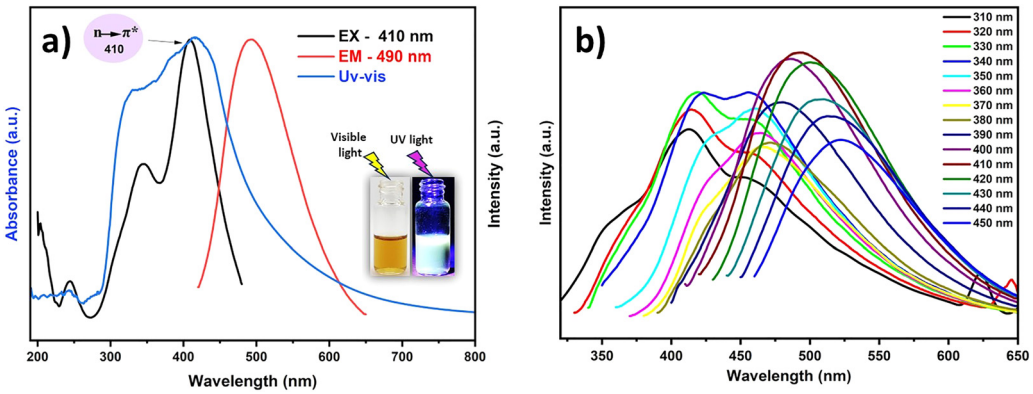

Fig. 5 Optical characterization of HHCDs: (a) UV-vis absorption (blue), excitation (black), and emission (red) spectra in ethanol, with an inset showing solution appearance under visible light (left) and 365 nm UV light (right); (b) excitation-wavelength-dependent emission spectra (310–450 nm in 10 nm increments).

The relatively narrow Stokes shift (80 nm) between absorption and emission maxima suggests efficient radiative recombination processes in the HHCDs.

The absolute quantum yield (QY) of the HHCDs was determined to be 4.49% using fluorescein (QY = 95%) as a reference standard. This QY value is moderate compared to some synthetic carbon dots and sufficient for photocatalytic applications.[83] The observed fluorescence properties stem from the combination of quantum confinement effects in the sp^2 carbon domains and surface state emissions from the functional groups, as evidenced by FTIR and NMR results.

3.3 Characterization of the TiO_2 nanocomposites (HH dye@TiO_2, HHCDs@TiO_2)

3.3.1 FTIR spectra analysis of the TiO_2 nanocomposites. The FTIR spectra of the nanocomposites confirm the successful incorporation of HH dye and HHCDs into the TiO_2 matrix (Fig. 6a–c). The spectrum of pure TiO_2 (Fig. 6a) displays a broad O–H stretching band at 3405 cm^{-1}, indicative of surface hydroxyl groups.[84] A band at 1656 cm^{-1} corresponds to Ti–OH bending,[84] while strong absorption bands at 715 cm^{-1} and 479 cm^{-1} are assigned to Ti–O–Ti lattice vibrations, characteristic of the anatase phase.[85]

The HH dye@TiO_2 nanocomposite (Fig. 6b) shows modified spectral features indicating successful hybridization. The O–H stretching shifts to 3398 cm^{-1}, suggesting hydrogen bonding between TiO_2 surface groups and HH dye molecules.[86] New peaks at 2923 cm^{-1} and 2867 cm^{-1} correspond to aliphatic C–H stretching vibrations from the HH dye components. The 1624 cm^{-1} region represents overlapping contributions from Ti–OH bending and aromatic C=C stretching from the dye's conjugated system.[87,88] The Ti–O vibrations shift slightly to 667 cm^{-1} and 470 cm^{-1}, demonstrating structural interactions between TiO_2 and HH dye functional groups without phase alteration.[89,90] More pronounced modifications appear in the HHCDs@TiO_2 spectrum (Fig. 6c). The O–H stretching intensifies and shifts to 3420 cm^{-1}, indicating enhanced surface hydroxylation.[91] Stronger C–H vibrations (2935 cm^{-1}, 2863 cm^{-1}) reflect greater organic surface coverage by HHCDs.

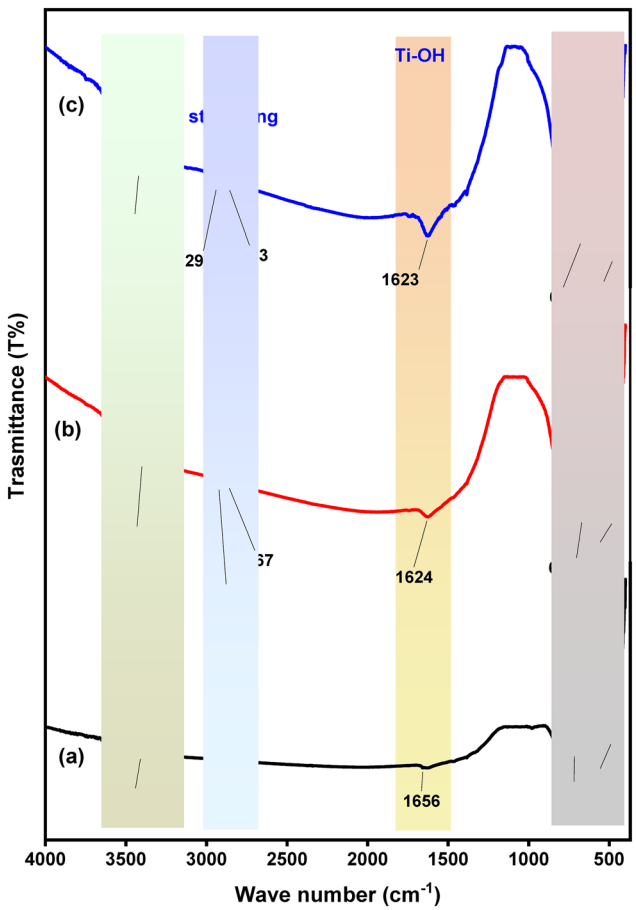

Fig. 6 FTIR spectra of (a) pure TiO_2, (b) HH dye@TiO_2 nanocomposites, and (c) HHCDs@TiO_2 nanocomposites.

The maintained anatase structure is evidenced by Ti–O vibrations at 669 cm^{-1} and 471 cm^{-1},[92] while the more intense 1623 cm^{-1} band suggests reinforced interfacial interactions between TiO_2 and HHCD surface groups.

These spectral changes collectively verify successful nanocomposite formation. The enhanced intensity and shifted

peaks in HHCDs@TiO_2 suggest stronger interfacial coupling compared to HH dye@TiO_2, which should facilitate improved visible-light absorption and charge carrier separation, crucial for enhancing Congo red photodegradation efficiency.

3.3.2 XRD analysis of the TiO_2 nanocomposites. X-ray diffraction analysis was conducted to examine the crystalline structure and phase composition of the prepared TiO_2-based photocatalysts. As shown in Fig. 7, the XRD patterns of the unmodified TiO_2 (anatase–rutile) (Degussa P25), HH-dye-modified TiO_2, and HHCD-modified TiO_2 nanocomposites all exhibit diffraction peaks matching the reference patterns for anatase (JCPDS No. 21-1272) and rutile (JCPDS No. 21-1276) phases.[93] This confirms that the fundamental crystalline structure of TiO_2 remains intact following surface modification with hollyhock-derived components.

Pure TiO_2 nanoparticles display characteristic peaks at 2θ values of 25.3°, 37.9°, 48.3°, 54.1°, 55.1°, 62.8°, 69.2°, 70.3°, and 75.4°, corresponding to the (101), (004), (200), (105), (211), (204), (116), (220), and (215) crystallographic planes of the tetragonal anatase phase, respectively.[94] The sharpness and high intensity of these peaks demonstrate the excellent crystallinity of the starting TiO_2 material. Both modified nanocomposites show nearly identical diffraction patterns to the unmodified TiO_2, with no detectable peak shifts or additional phases present.

The absence of distinct diffraction peaks attributable to either HH dye or HHCDs, despite the evidence of graphitic domains in HHCDs from HR-TEM analysis, is attributed to two primary factors.[95,96] First, the modifiers were loaded at a low weight ratio (10%) and are highly dispersed as a surface layer on the TiO_2 nanoparticles. Consequently, the X-ray scattering from these nanoscale components is overwhelmed by the intense diffraction from the bulk crystalline TiO_2 phase. Second, the broad, low-intensity (002) graphitic hump characteristic of HHCDs (centered around 22°) is effectively masked by the sharp, high-intensity peaks of the anatase and rutile phases. This is a common phenomenon when a small quantity of a semi-crystalline or amorphous material is composited with a highly crystalline substance, rendering the weaker signals undetectable.[97] This structural preservation confirms that the modification process does not alter the fundamental crystalline architecture of TiO_2 while still enabling surface functionalization.[98]

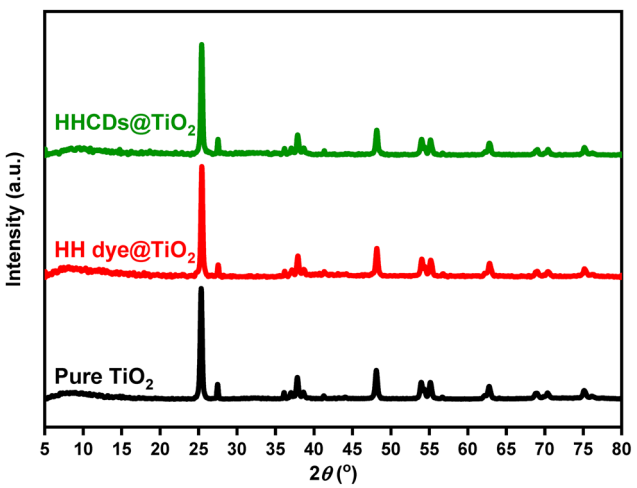

Fig. 7 XRD patterns comparing unmodified TiO_2 nanoparticles with HH dye@TiO_2, and HHCDs@TiO_2 nanocomposites, demonstrating the intact crystalline structure after surface modification.

The maintained crystallinity is particularly advantageous for photocatalytic applications as it ensures structural stability during photoreactions and preserves the intrinsic charge transport properties of TiO_2. Meanwhile, the surface modifications provide the additional benefit of enhanced visible-light absorption through the incorporated organic components, creating an optimal combination of crystalline stability and improved light harvesting capability for Congo red degradation.

3.3.3 FE-SEM and EDX analyses of TiO_2 nanocomposites. The surface morphology and elemental composition of the photocatalysts were investigated using FE-SEM and EDX. Fig. 8(a)–(c) presents the FE-SEM images and corresponding EDX spectra of the pristine TiO_2, HH dye@TiO_2, and HHCDs@TiO_2 nanocomposites. The FE-SEM images reveal that all samples maintain a spherical morphology, consistent with the characteristic shape of Degussa P25 TiO_2. However, the HHCDs@TiO_2 nanocomposite (Fig. 8c) shows a notably more compact surface texture with reduced porosity compared to both pure TiO_2 (Fig. 8a) and HH dye@TiO_2 (Fig. 8b), indicating successful surface modification through HHCD adsorption.[99]

EDX analysis provides quantitative evidence of the surface modifications. The pure TiO_2 spectrum (Fig. 8a) shows only titanium and oxygen signals, confirming the absence of impurities. In contrast, the HH dye@TiO_2 spectrum (Fig. 8b) reveals trace carbon content, while the HHCDs@TiO_2 spectrum (Fig. 8c) displays distinct peaks for carbon and nitrogen in addition to the primary Ti and O signals. As summarized in Table 1, the carbon content increases significantly from <0.0 wt% in pure TiO_2 to approximately 1.8 wt% in HH dye@TiO_2 and 8.74 wt% in HHCDs@TiO_2. Nitrogen is also detected, with concentrations of 1.3 wt% in the HH dye@TiO_2 and 7.91 wt% in HHCDs@TiO_2. This progressive increase in carbon content, particularly the substantial rise in HHCDs@TiO_2, confirms the effective surface deposition of organic components.[100]

The morphological and compositional changes observed through FE-SEM and EDX correlated well with the enhanced photocatalytic performance as can be seen in a later section. The increased carbon content provides more active sites for pollutant adsorption, while the nitrogen incorporation from HHCDs may introduce additional charge carrier trapping centers. The compact surface morphology of HHCDs@TiO_2 suggests improved interfacial contact between the carbon dots and TiO_2, which should facilitate more efficient charge transfer during photocatalysis. These structural modifications are expected to significantly enhance the visible-light photocatalytic degradation of Congo red compared to unmodified TiO_2.

3.4 Optical characterization of the TiO_2 nanocomposites

3.4.1 Optical band gap analysis. The optical band gap (OBG) of semiconductor materials, representing the energy

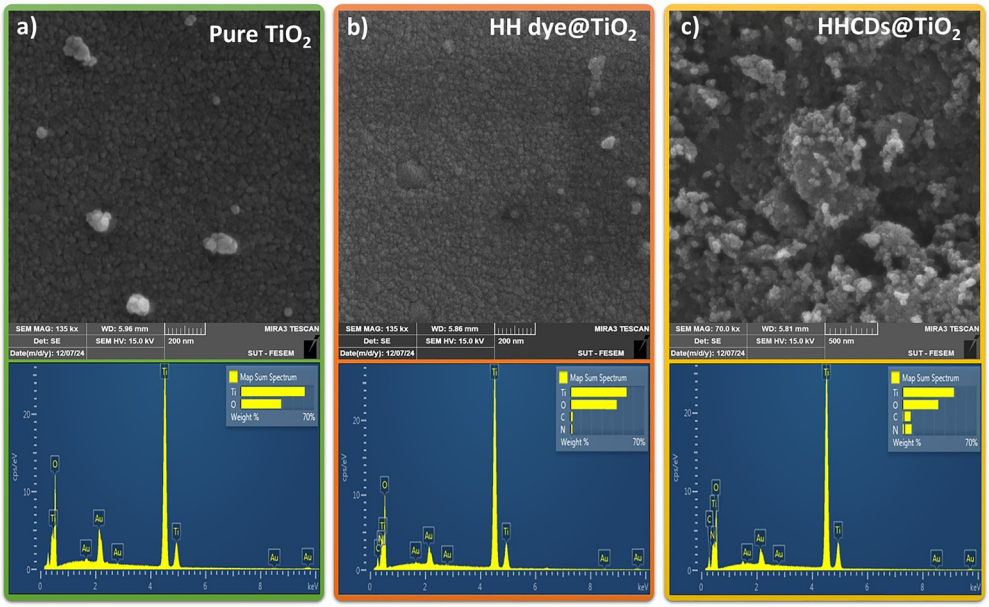

Fig. 8 FE-SEM images and corresponding EDX spectra of (a) pure TiO_2 nanoparticles, (b) HH dye@TiO_2, and (c) HHCDs@TiO_2 nanocomposites, showing morphological changes and elemental composition variations.

Table 1 The main elements and chemical composition of pure TiO_2 and the HH dye@TiO_2 and HHCDs@TiO_2 composites from EDX results

Catalyst	Element	Weight%	Atomic%
TiO_2	O	38.79	65.49
	Ti	61.21	34.51
	Total	**100**	**100**
HH dye@TiO_2	C	1.8	4.14
	N	1.3	2.86
	O	43.6	57.12
	Ti	53.3	35.88
	Total	**100**	**100**
HHCDs@TiO_2	C	8.74	5.4
	N	7.91	3.32
	O	34.1	54.04
	Ti	49.25	37.24
	Total	**100**	**100**

required for electron excitation from the valence to conduction band, fundamentally determines their photophysical and photocatalytic properties. The Tauc plot analysis of UV-vis diffuse reflectance spectra (DRS) was employed to determine the OBG values for pure TiO_2, HH dye@TiO_2, and HHCDs@TiO_2 nanocomposites.[101]

The analysis utilizes the Tauc relation:

$$(\alpha h\nu)^n = B(h\nu - E_g) \quad (3)$$

where α is the absorption coefficient, $h\nu$ is the photon energy, B is a constant, and n represents the transition type (n = 2 for direct, n = 1/2 for indirect transitions).[102] For powder samples, the Kubelka–Munk function transforms reflectance data:

$$F(R) = (1 - R)^2/2R \quad (4)$$

where R is the measured reflectance.[103]

Fig. 9 presents the DRS spectra plotted as $F(R)$ *versus* wavelength. Modified TiO_2 samples showed reduced reflectance compared to pure TiO_2, particularly in the visible region, indicating enhanced light absorption.[104] The Tauc plots derived from these spectra (Fig. 10a and b) reveal distinct optical transitions. Linear extrapolation yields direct OBG values of 3.25 eV (pure TiO_2), 3.08 eV (HH dye@TiO_2), and 2.89 eV (HHCDs@TiO_2), and indirect OBG values of 2.93 eV, 2.67 eV, and 1.3 eV for pure and doped TiO_2 samples, respectively (Table 2).

The progressive OBG narrowing demonstrates successful modification of TiO_2's electronic structure. The 0.36 eV

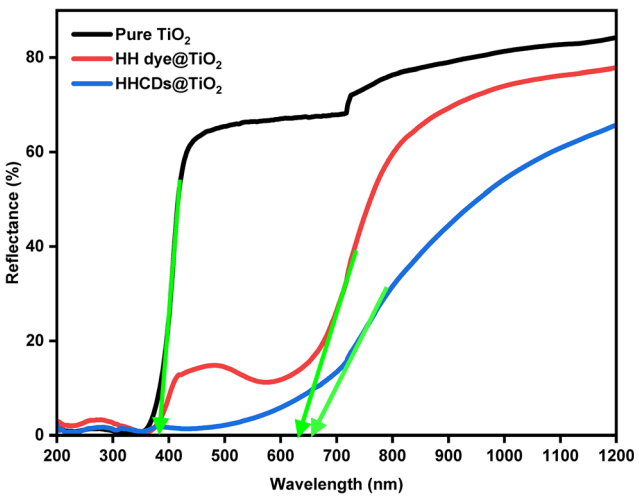

Fig. 9 UV-vis diffuse reflectance spectra (Kubelka–Munk function) of pure and modified TiO_2 photocatalysts, showing enhanced visible-light absorption for the nanocomposites.

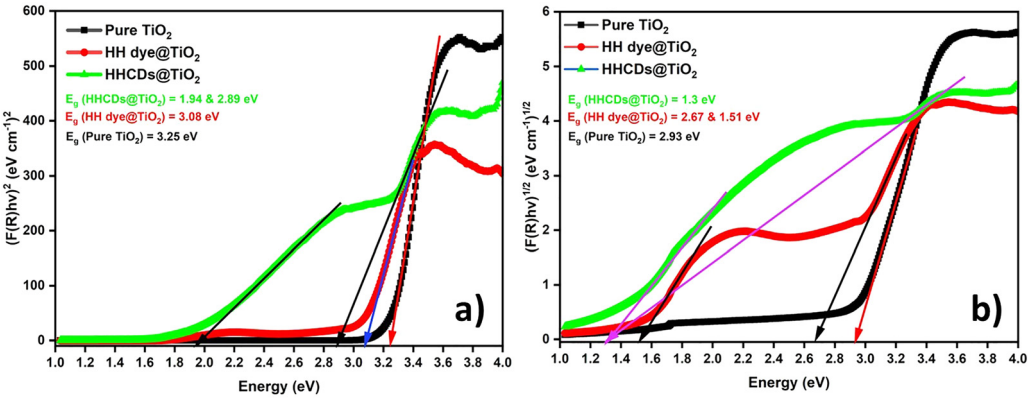

Fig. 10 Tauc plots for (a) direct (n = 2) and (b) indirect (n = 1/2) bandgap determination through linear extrapolation.

Table 2 Experimentally determined optical band gaps and trapping levels for pure TiO_2, HH@TiO_2, and HHCDs@TiO_2 photocatalysts

Transition	Catalysts	Trapping level (eV)	OBG energy (eV)
$(F(R) \times h\nu)^2$	Pure TiO_2	—	3.25
	HH dye@TiO_2	—	3.08
	HHCDs@TiO_2	1.94	2.89
$(F(R) \times h\nu)^{1/2}$	Pure TiO_2	—	2.93
	HH dye@TiO_2	1.51	2.67
	HHCDs@TiO_2	1.3	1.3

reduction in direct bandgap for HHCDs@TiO_2 confirms improved visible-light absorption, while the exceptionally low indirect bandgap (1.3 eV) suggests the introduction of mid-gap states that facilitate charge carrier generation.[105] These defect states, evidenced by trapping levels between 1.3 and 1.94 eV, act as "stepping stones" inside the gap, which separates the VB from the CB and thus will enhance the photocatalytic efficiency under visible light.

3.4.2 Zeta potential analysis of pure and modified TiO_2 photocatalysts. Zeta potential measurements provide critical insights into the colloidal stability and surface charge characteristics of nanoparticle dispersions.[106] Our systematic evaluation using dynamic light scattering (DLS) revealed that both modified TiO_2 photocatalysts exhibit excellent colloidal stability in aqueous media. The measurements were conducted under controlled conditions with deionized water as the dispersion medium (viscosity = 0.893 mPa s at 25.10 °C), conductivity values of 0.066–0.072 mS cm^{-1}, and applied electrode voltages of 3.8–3.9 V. The strongly negative zeta potentials of −52.1 mV for HH dye@TiO_2 and −45.0 mV for HHCDs@TiO_2 (Fig. 11a and c) demonstrate substantial electrostatic repulsion between particles, effectively preventing agglomeration. For comparison, pure TiO_2 nanoparticles synthesized using this sol–gel method typically exhibit zeta potential values in the range of −40 to −45 mV.[107,108] This observation confirms that the surface modifications successfully enhanced the surface charge and colloidal stability of the composite photocatalysts.

Complementary electrophoretic mobility measurements yielded values of −0.000404 $cm^2\ V^{-1}\ s^{-1}$ and −0.000349 $cm^2\ V^{-1}\ s^{-1}$ for HH dye@TiO_2 and HHCDs@TiO_2, respectively (Fig. 11b and d). These negative values confirm the overall negative surface charge of the photocatalysts, with the modest magnitude

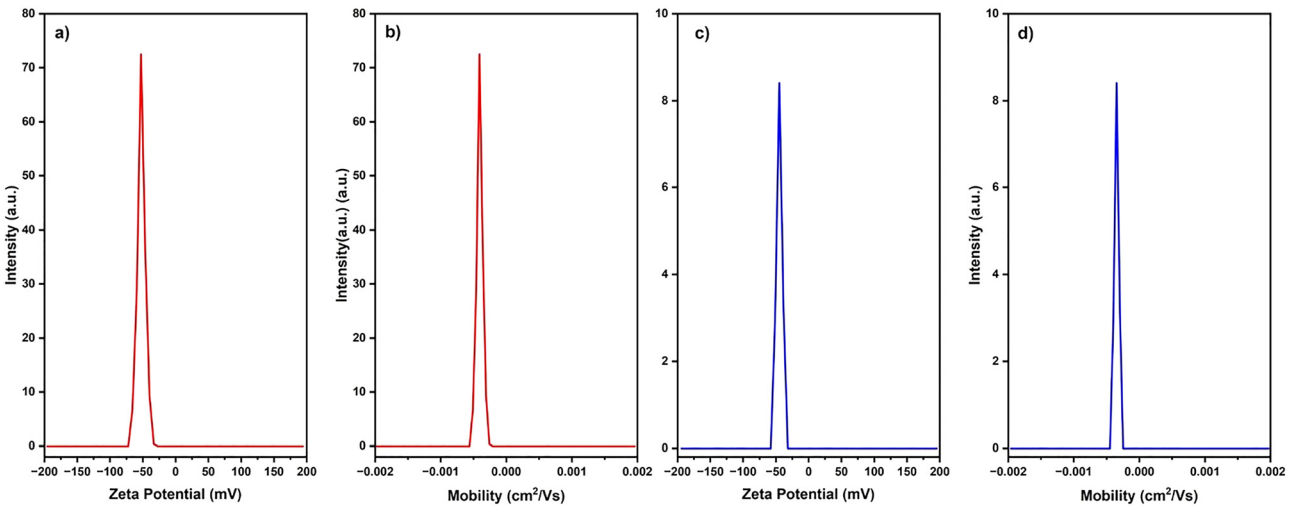

Fig. 11 (a) and (c) The zeta potential and (b) and (d) the electrophoretic mobility of HH dye@TiO_2 and HHCDs@TiO_2, respectively.

indicating controlled migration under applied electric fields. The surface charge originates primarily from anionic functional groups introduced through modification, including carboxyl (–COOH) groups from hollyhock-derived components, surface hydroxyl (–OH) moieties, and amino ($–NH_2$) groups present in the carbon dot structures. These functional groups collectively enhance both surface charge density and aqueous dispersibility.[107]

These results demonstrate that both nanocomposites exhibit high negative zeta potentials and superior colloidal stability, indicating enhanced surface coverage by the adsorbed dye molecules compared to unmodified TiO_2. This improved stability is particularly advantageous for photocatalytic applications as it maintains uniform dispersion of active sites, prolongs interaction with target pollutants, prevents performance-degrading aggregation, and facilitates efficient light absorption throughout the reaction medium. The robust colloidal stability demonstrated by these measurements confirms the successful surface modification of TiO_2 and predicts favorable performance in aqueous photocatalytic degradation of Congo red.

3.5 Photocatalytic activity of TiO_2 nanocomposites for CR degradation

3.5.1 Effect of catalyst dosage on CR degradation. The influence of catalyst dosage on photodegradation efficiency is a critical parameter for practical applications. To investigate this, various amounts of HH dye@TiO_2 and HHCDs@TiO_2 (0.02, 0.03, 0.04, 0.05, 0.06, and 0.07 g) were tested under identical conditions: initial CR concentration of 5 ppm, neutral pH (6.21), and 60 min visible-light irradiation. Fig. 12 demonstrates that degradation efficiency initially increases with catalyst dosage, reaching optimal performance at 60 mg for HH dye@TiO_2 (achieving 97% degradation) and 40 mg for HHCDs@TiO_2 (exceeding 99.9% degradation).

Beyond these optimal loadings, distinct behaviors emerged between the two catalysts. HH dye@TiO_2 exhibited reduced efficiency at higher dosages. Various interpretations have been introduced in the literature to explain this phenomenon, such as excessive catalyst loading increases suspension opacity, significantly limiting light penetration and photon absorption. Second, catalyst agglomeration at elevated concentrations reduces the availability of active sites for both dye adsorption and surface reactions. Third, light scattering effects become more pronounced, with aggregated particles potentially deactivating excited molecules through collisions with ground-state species.

In contrast, HHCDs@TiO_2 maintained stable photocatalytic performance even at higher dosages. This remarkable stability suggests that the carbon dot modification effectively enhances catalyst dispersibility and optimizes light utilization, thereby mitigating the common limitations observed with conventional modified TiO_2. These findings align well with established literature reporting optimal TiO_2 loadings in the range of 400–500 mg L^{-1},[109,110] while simultaneously highlighting the superior performance characteristics of our carbon dot-modified photocatalyst under visible light conditions.

The observed performance differences between the two catalysts underscore the significant advantages conferred by carbon dot modification. The HHCDs@TiO_2 nanocomposite not only achieves higher maximum degradation efficiency ($>99.9\%$ *vs.* 97%) but also demonstrates greater stability across a wider range of catalyst loadings. This enhanced performance profile suggests that the carbon dot modification successfully addresses key limitations typically associated with TiO_2-based photocatalysts, particularly regarding light absorption efficiency and particle dispersion at higher concentrations.

3.5.2 Effect of initial CR concentration on photodegradation efficiency. The influence of initial dye concentration on

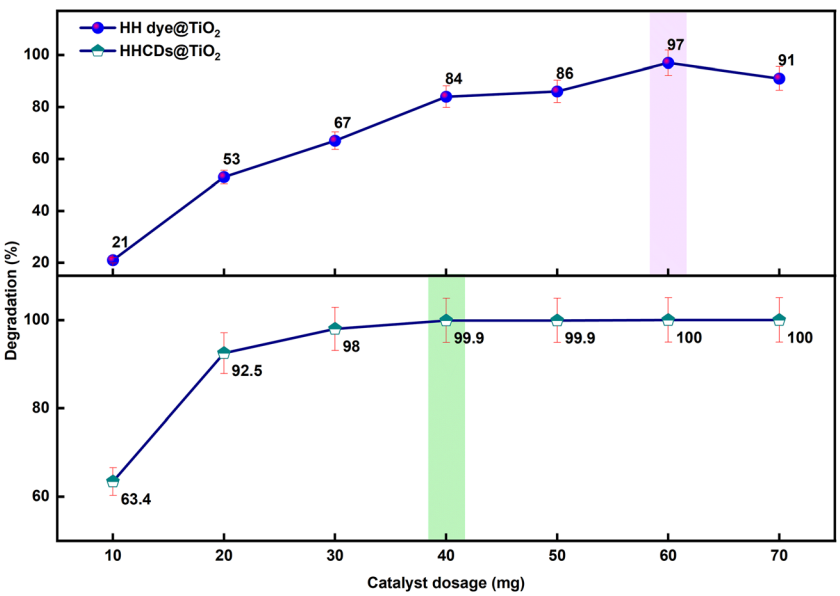

Fig. 12 Photodegradation efficiency of CR (5 ppm) under visible light (60 min) as a function of HH dye@TiO_2 and HHCDs@TiO_2 dosage.

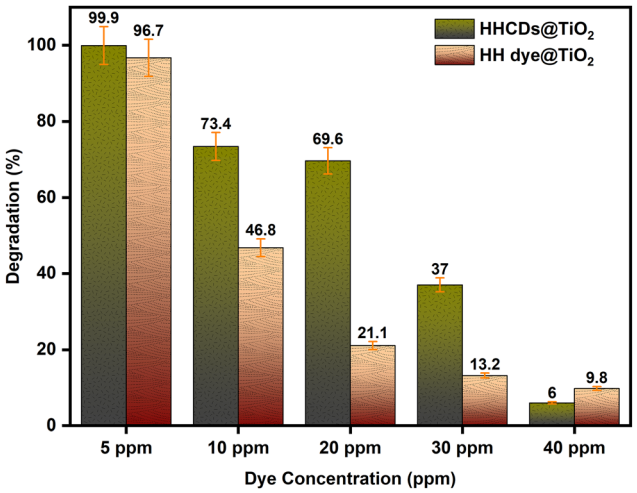

Fig. 13 Photodegradation efficiency of HH dye@TiO_2 and HHCDs@TiO_2 as a function of initial CR concentration under visible-light irradiation (60 min, unadjusted pH, optimum catalyst dosages).

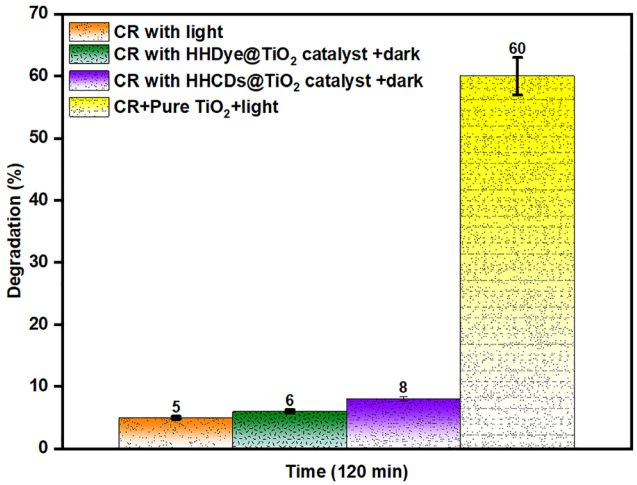

Fig. 14 Comparative analysis of CR (10 ppm) degradation efficiency after 120 minutes under four experimental conditions: visible light only, HH dye@TiO_2 in darkness, HHCDs@TiO_2 in darkness, and pure TiO_2 under visible light at unadjusted pH.

photocatalytic degradation was systematically investigated using CR solutions ranging from 5 to 40 ppm. As illustrated in Fig. 13, both photocatalysts exhibited a clear inverse relationship between initial concentration and degradation efficiency, with HHCDs@TiO_2 demonstrating consistently superior performance across all tested concentrations. The carbon HHCDs@TiO_2 photocatalyst achieved remarkable degradation rates of 99.9%, 73.4%, 69.6%, 37%, and 6% at 5, 10, 20, 30, and 40 ppm, respectively, which is superior to the HH dye@TiO_2 system (96.7%, 46.8%, 21.1%, 13.2%, and 9.8% at the corresponding concentrations). This concentration-dependent behavior can be attributed to several interrelated factors governing the photocatalytic process.[111–113] At higher dye concentrations, several limiting effects become pronounced. For example, an increased number of dye molecules competes for adsorption on active sites, reducing the available surface area for photon absorption and radical generation. Moreover, the solution's optical density increases, limiting light penetration and consequently the production of reactive oxygen species ($^{\bullet}OH$ and $^{\bullet}O_2^-$) will drop, and finally intermediate degradation products may occupy active sites, further inhibiting the photocatalytic process.

The superior performance of HHCDs@TiO_2, particularly evident at intermediate concentrations (10–20 ppm), suggests that the carbon dot modification enhances the catalyst's ability to maintain active site accessibility and light absorption efficiency even in the presence of competing dye molecules.

3.5.3 Evaluation of CR degradation under various conditions. The photocatalytic performance of the synthesized TiO_2-based catalysts was systematically evaluated under different experimental conditions, as summarized in Fig. 14. Control experiments established important baseline measurements for CR degradation mechanisms. Under visible light irradiation alone (without any photocatalyst), only 5% degradation of CR was observed after 120 minutes, confirming the dye's remarkable stability to direct photolysis under these conditions.

To assess the adsorption capacity of the photocatalysts, experiments were conducted in complete darkness using optimal dosages of HH dye@TiO_2 and HHCDs@TiO_2 with 10 ppm CR solutions. Both catalysts showed minimal activity, with degradation efficiencies of just 6% and 8%, respectively, after 120 minutes, demonstrating that adsorption plays a negligible role in the overall degradation process.

The performance of pure TiO_2 under visible light irradiation resulted in 60% CR degradation, confirming that the TiO_2 efficiency remains limited. The dark control experiment establishes that the observed dye removal is primarily due to photocatalytic degradation rather than adsorption.

3.5.4 Time analysis of photocatalytic degradation. The kinetics of CR degradation were systematically investigated using both modified photocatalysts under optimized conditions: 60 mg HH dye@TiO_2 and 40 mg HHCDs@TiO_2 at pH 5.75 (unadjusted) with 10 ppm CR under visible light irradiation. As shown in Fig. 15, both photocatalysts demonstrated effective degradation capabilities, though with significantly different kinetic profiles.

The HH dye@TiO_2 system achieved 98.6% degradation after 140 minutes, with the reaction kinetics showing substantial slowing beyond 120 minutes (96.8% degradation). In striking contrast, the HHCDs@TiO_2 nanocomposite exhibited markedly faster degradation kinetics, reaching 97.1% efficiency in 80 minutes. The accompanying UV-vis spectra (Fig. 15 inset) corroborate these temporal trends, showing progressive diminution of the characteristic CR absorption peaks.

This dramatic enhancement in the photocatalytic performance of the HHCDs@TiO_2 nanocomposite can be attributed to the synergistic effects of an expanded visible light absorption range, improved charge carrier separation efficiency, and an increased number of active surface sites.[114,115] The HHCDs@TiO_2 composite degrades the CR dye in approximately half the time required by the HH dye@TiO_2 composite. This

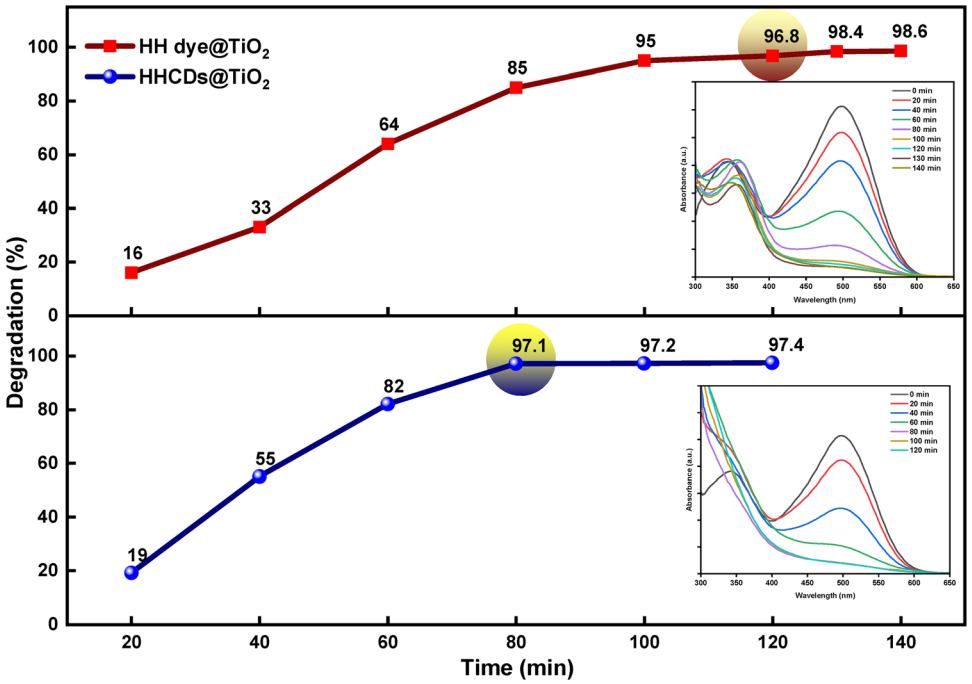

Fig. 15 Time evolution of CR degradation using HH dye@TiO_2 and HHCDs@TiO_2 under visible light irradiation, showing 96.8% degradation at 120 min for HH dye@TiO_2 and 97.1% degradation at 80 min for HHCDs@TiO_2. The insets display the corresponding UV-vis spectral changes documenting the photocatalytic process.

accelerated kinetics underscores the significant advantage of incorporating CDs into photocatalytic materials, which is particularly critical for time-sensitive wastewater treatment applications that demand rapid pollutant removal.

3.5.5 Effect of solution pH on photocatalytic efficiency. The influence of solution pH on CR degradation efficiency was systematically examined across a pH range from 4.17 to 8.7, as illustrated in Fig. 16. All experiments were conducted under controlled conditions: optimal catalyst dosages (60 mg HH dye@TiO_2 and 40 mg HHCDs@TiO_2), 120 minutes of visible light irradiation, and 10 ppm CR concentration. The pH adjustment was carefully performed using 0.1 M HCl and 0.1 M NaOH solutions.

The photocatalytic systems exhibited maximum efficiency in strong acidic conditions (pH 4.17), achieving remarkable degradation rates of 99% for HH dye@TiO_2 and 93.3% for HHCDs@TiO_2 nano-composites. The enhanced performance of dye-doped TiO_2 could be attributed to two reasons: (1) the protonation of TiO_2 surface groups in acidic media creates a positive surface charge that promotes electrostatic attraction and subsequent adsorption of anionic CR molecules, and (2) the abundance of H^+ ions facilitates the generation of reactive oxygen species, thereby accelerating the degradation process.[116,117]

As the pH increased towards alkaline conditions, we observed a substantial decrease in degradation efficiency, with minimum values of 12% (HH dye@TiO_2) and 32.1% (HHCDs@TiO_2) at pH 8.7. This dramatic reduction results from surface deprotonation of the photocatalysts, leading to negative surface charges that electrostatically repel the anionic dye molecules. Meanwhile, a slight increase in degradation was noted in the alkaline region, potentially due to hydroxyl radical-mediated oxidation.[118] This effect was relatively insignificant compared to the dominant electrostatic interactions.

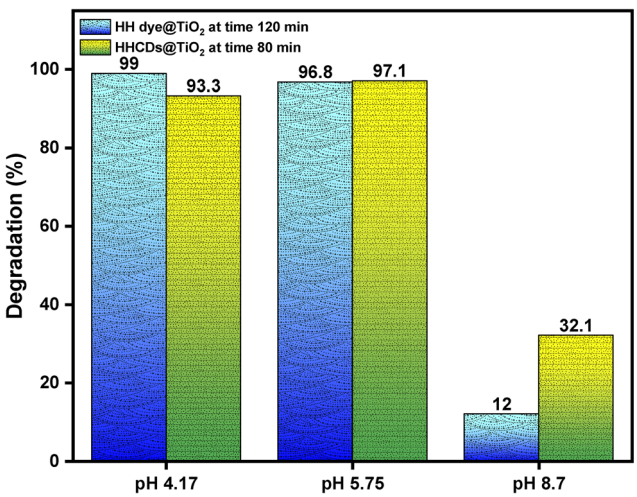

Fig. 16 pH-dependent photocatalytic degradation of the CR dye using HHdye@TiO_2 and HHCDs@TiO_2 under visible light irradiation (initial dye concentration: 10 ppm; optimal catalyst dosage; irradiation times: 120 min for HH dye@TiO_2 and 80 min for HHCDs@TiO_2, respectively).

These findings demonstrate that the solution pH is a critical parameter controlling photocatalytic efficiency, with acidic to

near-neutral conditions (pH 4.17–7) proving most favorable for anionic dye degradation. The superior performance of both photocatalysts in acidic media underscores the importance of surface charge characteristics and reactive species generation in the photocatalytic mechanism.

3.5.6 Stability and reusability assessment of the photocatalysts. The long-term stability and reusability of photocatalysts are critical parameters for practical wastewater treatment applications. To evaluate these characteristics, both HH dye@TiO_2 and HHCDs@TiO_2 were subjected to five consecutive photocatalytic cycles under visible light irradiation while maintaining identical experimental conditions for CR degradation.

As demonstrated in Fig. 17, both photocatalysts exhibited excellent operational stability throughout the testing period. HHCDs@TiO_2 showed particularly remarkable durability, with only a minimal reduction in degradation efficiency from 99% to 97% after five cycles. Similarly, HH dye@TiO_2 maintained good stability, with its efficiency decreasing modestly from 97% to approximately 90% over the same number of cycles.

The slight decline in performance observed for both materials can be attributed to several factors:[119,120] (1) inevitable physical loss of the catalyst material during recovery and washing processes between cycles, (2) potential accumulation of degradation byproducts on active sites, and (3) possible gradual structural changes in the photocatalysts with repeated use. Notably, the superior retention of activity by HHCDs@TiO_2 suggests that the carbon dot modification may provide enhanced protection against these degradation mechanisms.

These results confirm that both modified photocatalysts, particularly the carbon dot-enhanced HHCDs@TiO_2, possess the durability required for sustainable water treatment applications. The maintained high performance over multiple cycles indicates excellent potential for long-term use in practical environmental remediation scenarios.

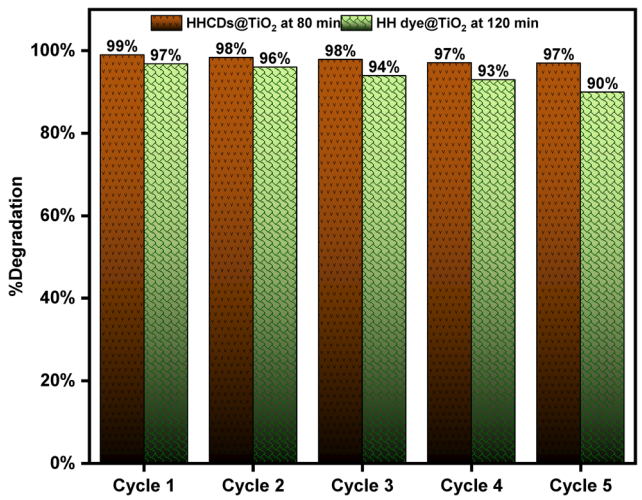

Fig. 17 Cyclic stability test of the HH dye@TiO_2 and HHCDs@TiO_2 photocatalysts for CR degradation over five consecutive uses under visible light irradiation.

3.6 Mechanistic insights into photocatalytic degradation pathways

The photocatalytic degradation mechanism of Congo red was systematically investigated through radical scavenging experiments using both HH dye@TiO_2 and HHCDs@TiO_2 nanocomposites under visible light irradiation. Initial dark control experiments confirmed the essential light dependence of the process, with minimal degradation observed without illumination. To identify the active species responsible for dye degradation, we employed a series of specific scavengers targeting different reactive oxygen species and charge carriers (Table 3).

The scavenging experiments revealed distinct patterns of reactivity for each photocatalyst system. When the electron scavenger ($AgNO_3$) was introduced,[121] the degradation efficiency dropped significantly to 33% for HH dye@TiO_2 and 27% for HHCDs@TiO_2, demonstrating the crucial role of photogenerated electrons in both systems. The addition of a hole scavenger (KI) caused more moderate reductions to 89.4% and 89.0%, respectively, indicating that while holes contribute to the process, their role is less dominant compared to electrons. These results collectively establish that charge separation and subsequent electron transfer represent key steps in the photocatalytic mechanism.

The investigation of reactive oxygen species provided particularly valuable insights into the degradation pathways. The dramatic suppression of degradation efficiency observed with hydroxyl radical scavenger (vitamin C), reducing activity to just 4.1% for HH dye@TiO_2 and 15.6% for HHCDs@TiO_2, unequivocally identifies $^{\bullet}OH$ as the predominant oxidative species. This finding is complemented by the significant but less severe inhibition observed with singlet oxygen scavenger (L-histidine), which decreased degradation to 27.9% and 36.6%, respectively, confirming a secondary role for $^1O_2$ in the process. In contrast, the minimal effect of superoxide scavenger (*p*-benzoquinone) suggests that $^{\bullet}O_2^-$ radicals contribute negligibly to the overall degradation mechanism.

These experimental results support a proposed mechanism where visible light excitation generates electron–hole pairs in both photocatalyst systems. The photogenerated electrons participate in limited oxygen reduction, while the holes either directly oxidize dye molecules or react with surface hydroxyl

Table 3 A comprehensive quantitative summary of the scavenging experiments, clearly demonstrating the relative contributions of different reactive species in each photocatalyst system

Reactive species	Scavengers	Equivalent	Degradation (%) using HH dye@TiO_2 at 120 min	Degradation (%) using HHCDs@TiO_2 at 90 min
	Standard (no scavengers)		97	99
	Dark		Trace	Trace
e^-	$AgNO_3$	2	33	27.5
h^+	KI	1	89.4	88.97
$^1O_2$	L-Histidine	1	27.9	36.6
$^{\bullet}OH$	VC	1	4.1	15.6
$^{\bullet}O_2^-$	*p*-Bq	1	Trace	Trace

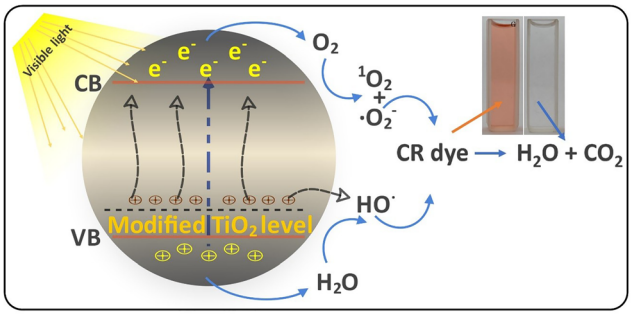

Fig. 18 Proposed mechanistic pathways for CR degradation by modified TiO_2 nanocomposites.

groups/water to produce highly reactive •OH radicals.[122] The HHCDs@TiO_2 appears to facilitate a more balanced contribution from multiple reactive species (•OH, e^-, and $^1O_2$), explaining its enhanced photocatalytic efficiency compared to HH dye@TiO_2, where •OH radicals dominate the oxidation process. The superior performance of HHCDs@TiO_2 likely stems from improved charge separation and additional reactive pathways enabled by the carbon dot modification.

Fig. 18 illustrates the proposed mechanistic pathways, beginning with light-induced excitation of electrons from the valence band (VB) to the conduction band (CB) or mid-gap states, generating electron–hole pairs. The photogenerated electrons participate in limited oxygen reduction to form $^{\bullet}O_2^-$, while the holes either directly oxidize dye molecules or react with surface-adsorbed water/hydroxyl groups to produce •OH radicals. These reactive species, along with $^1O_2$, collectively mediate the oxidative degradation of Congo red into CO_2 and H_2O. The photocatalytic degradation of CR is a complex process that proceeds through the cleavage of the azo bonds, generating intermediate organic compounds such as benzidine derivatives, followed by further ring opening and eventual mineralization to CO_2, H_2O, and inorganic ions.[123,124] The collective evidence from these experiments provides a robust foundation for understanding the enhanced photocatalytic behavior of these modified TiO_2 systems and their potential applications in wastewater treatment.

4. Conclusion

In conclusion, this study successfully demonstrates the development of sustainable TiO_2 nanocomposites modified with hollyhock-derived natural dye (HH dye) and carbon dots (HHCDs) for the efficient visible-light degradation of Congo red (CR). Comprehensive characterization confirmed the successful formation of the composites and their enhanced optoelectronic properties. A critical finding was the significant narrowing of the direct optical bandgap from 3.25 eV for pure TiO_2 to 3.08 eV for HH dye@TiO_2 and further to 2.89 eV for HHCDs@TiO_2, which directly correlated with enhanced visible-light absorption. Photocatalytic performance under visible light revealed the superior activity of the HHCDs@TiO_2 composite, which achieved 97.1% degradation of 10 ppm CR in just 80 minutes, outperforming the HH dye@TiO_2 composite that required 120 minutes to reach 96.8% degradation.

Systematic optimization identified the optimal catalyst dosage to be 0.06 g for HH dye@TiO_2 and a lower, more efficient loading of 0.04 g for HHCDs@TiO_2. The degradation efficiency was highly dependent on solution pH, with strongly acidic conditions (pH 4.17) proving most favorable, yielding remarkable degradation rates of 99% and 93.3% for HH dye@TiO_2 and HHCDs@TiO_2, respectively. Furthermore, both photocatalysts exhibited excellent operational stability, with the HHCDs@TiO_2 nanocomposite showing exceptional reusability by retaining over 97% of its initial efficiency after five consecutive cycles. Mechanistic investigations through scavenging experiments unequivocally identified hydroxyl radicals as the predominant oxidative species, with the carbon dot modification in HHCDs@TiO_2 facilitating more effective charge separation.

This work establishes a green protocol for valorizing hollyhock floral waste into high-performance photocatalysts. The direct comparison reveals that carbon dot modification offers superior benefits over the natural dye alone, particularly in enhancing reaction kinetics and charge separation. The HHCDs@TiO_2 composite, with its rapid degradation kinetics, high efficiency, and remarkable stability, emerges as a highly promising and sustainable candidate for solar-driven wastewater treatment, advancing the principles of a circular economy and green chemistry.

Conflicts of interest

The authors declare that they have no known competing financial interests or personal relationships that could have appeared to influence the work reported in this paper.

Data availability

Data will be made available on request.

Acknowledgements

The authors thank the University of Sulaimani for its scientific support in accomplishing this research.

References

1 L. Wang, L. Zhao, D. Si, Z. Li, H. An, H. Ye, Q. Xin, H. Li and Y. Zhang, *Sep. Purif. Technol.*, 2024, **331**, 125571.
2 S. I. Siddiqui, E. S. Allehyani, S. A. Al-Harbi, Z. Hasan, M. A. Abomuti, H. K. Rajor and S. Oh, *Processes*, 2023, **11**, 807.
3 V. Vaiano and I. De Marco, *Separations*, 2023, **10**, 230.
4 A. Thakur, A. Kumar and A. Singh, *Carbon*, 2024, **217**, 118621.
5 R. Ahmad and R. Kumar, *Appl. Surf. Sci.*, 2010, **257**, 1628–1633.

6 E. D'Souza, A. B. Fulke, N. Mulani, A. Ram, M. Asodekar, N. Narkhede and S. N. Gajbhiye, *Environ. Earth Sci.*, 2017, **76**, 721.
7 S. Wafiroh, A. Abdulloh and A. A. Widati, *Chem. Chem. Technol.*, 2021, **15**, 291–298.
8 A. Ahmad, S. H. Mohd-Setapar, C. S. Chuong, A. Khatoon, W. A. Wani, R. Kumar and M. Rafatullah, *RSC Adv.*, 2015, **5**, 30801–30818.
9 F. A. Zahrandika, S. Adityosulindro, S. N. Felia and K. Kusrestuwardhani, *E3S Web Conf.*, 2024, **485**, 02006.
10 R. A. El-Salamony, E. Amdeha, A. M. El Shafey and A. M. Al Sabagh, *Int. J. Environ. Anal. Chem.*, 2023, **103**, 868–883.
11 J. Zhang, P. Zhou, J. Liu and J. Yu, *Phys. Chem. Chem. Phys.*, 2014, **16**, 20382–20386.
12 T. Chen, W.-L. Chen, B. J. Foley, J. Lee, J. P. C. Ruff, J. Y. P. Ko, C. M. Brown, L. W. Harriger, D. Zhang, C. Park, M. Yoon, Y.-M. Chang, J. J. Choi and S.-H. Lee, *Proc. Natl. Acad. Sci. U. S. A.*, 2017, **114**, 7519–7524.
13 Q. Wang, J. Qiao and J. Zhou, *ECS J. Solid State Sci. Technol.*, 2014, **3**, Q157–Q161.
14 J. Wang, Z. Wang, W. Wang, Y. Wang, X. Hu, J. Liu, X. Gong, W. Miao, L. Ding, X. Li and J. Tang, *Nanoscale*, 2022, **14**, 6709–6734.
15 M. Ghosh, P. Chowdhury and A. K. Ray, *Catalysts*, 2020, **10**, 917.
16 A. H. Zyoud, F. Saleh, M. H. Helal, R. Shawahna and H. S. Hilal, *J. Nanomater.*, 2018, **2018**, 1–14.
17 C. Lin, Q. Xia, K. Li, J. Li and Z. Yang, *J. Korean Phys. Soc.*, 2018, **72**, 1307–1312.
18 G. H. Hamasalih, S. J. Mohammed and S. B. Aziz, *J. Sol-Gel Sci. Technol.*, 2025, **116**, 1142–1166.
19 Y. Tanaka, N. Sasaki and A. Ohmiya, *Plant J.*, 2008, **54**, 733–749.
20 S. B. Aziz, D. M. Aziz, D. S. Muhammad, P. O. Hama, D. Q. Muheddin, S. Al-Zangana, A. M. Huseein, G. H. Hamasalih, A. H. A. Darwesh and O. G. Abdullah, *J. Inorg. Organomet. Polym. Mater.*, 2025, **35**, 2109–2125.
21 Z. Ma, H. Ming, H. Huang, Y. Liu and Z. Kang, *New J. Chem.*, 2012, **36**, 861.
22 W. Wang, L. Cheng and W. Liu, *Sci. China: Chem.*, 2014, **57**, 522–539.
23 D. Bhattacharya, M. K. Mishra and G. De, *J. Phys. Chem. C*, 2017, **121**, 28106–28116.
24 A. Emanuele, S. Cailotto, C. Campalani, L. Branzi, C. Raviola, D. Ravelli, E. Cattaruzza, E. Trave, A. Benedetti, M. Selva and A. Perosa, *Molecules*, 2019, **25**, 101.
25 B. Zhang, H. Maimaiti, D.-D. Zhang, B. Xu and M. Wei, *J. Photochem. Photobiol., A*, 2017, **345**, 54–62.
26 H. Zhang, H. Huang, H. Ming, H. Li, L. Zhang, Y. Liu and Z. Kang, *J. Mater. Chem.*, 2012, **22**, 10501.
27 C. Praharaj, Saloni, G. K. Patel and S. Nara, *Ind. Crops Prod.*, 2025, **230**, 121074.
28 S. Raja, G. T. S. T. da Silva, S. Anbu, C. Ribeiro and L. H. C. Mattoso, *Biomass Convers. Biorefin.*, 2024, **14**, 21925–21937.
29 H. Radi, K. F. El-Nemr, S. M. Elmesallamy and E. Amdeha, *Pigm. Resin Technol.*, 2025, **54**, 561–570.
30 E. Amdeha, *Topics in Mining, Metallurgy and Materials Engineering*, Springer Science and Business Media Deutschland GmbH, 2021, pp. 385–417.
31 E. Amdeha, *Diversity and Applications of New Age Nanoparticles*, IGI Global, 2023, pp. 112–154.
32 J. Fan, L. Kang, X. Cheng, D. Liu and S. Zhang, *Nanomaterials*, 2022, **12**, 4473.
33 G. Náthia-Neves, Á. L. Santana, J. Viganó, J. Martínez and M. A. A. Meireles, *Processes*, 2021, **9**, 1435.
34 A. Ghorbani, G. Eghlima, M. Farzaneh and A. Rezghiyan, *BMC Plant Biol.*, 2025, **25**, 478.
35 N. F. S. Daud, F. M. Said, M. Ramu and N. M. H. Yasin, *IOP Conf. Ser.:Mater. Sci. Eng.*, 2020, **736**, 022084.
36 K. Saeed, I. Khan, T. Gul and M. Sadiq, *Appl. Water Sci.*, 2017, **7**, 3841–3848.
37 M. Grabolle, M. Spieles, V. Lesnyak, N. Gaponik, A. Eychmüller and U. Resch-Genger, *Anal. Chem.*, 2009, **81**, 6285–6294.
38 N. A. Abdel-salam, N. M. Ghazy, S. M. Sallam, M. M. Radwan, A. S. Wanas, M. A. ElSohly, M. A. El-Demellawy, N. M. Abdel-Rahman, S. Piacente and M. L. Shenouda, *Nat. Prod. Res.*, 2018, **32**, 702–706.
39 A. Safari, M. Rahimi, A. Sonboli, H. Behboudi and S. Nejad Ebrahimi, *Ind. Crops Prod.*, 2024, **222**, 119944.
40 A. M. Babatimehin, O. E. Ogunbamowo, G. O. Ajayi, A. El Gamal, T. Bin Emran, E. A. Ofudje and M. Hefnawy, *BioResources*, 2025, **20**, 6948–6965.
41 S. B. Aziz, D. S. Muhammad, S. J. Mohammed, D. Q. Muheddin, S. Al-Zangana, A. M. Hussein, A. R. Murad, G. H. Hamasalih, S. M. Hamad and D. Shaikhah, *J. Mater. Sci.:Mater. Eng.*, 2025, **20**, 86.
42 A. Ebrahiminezhad, V. Varma, S. Yang, Y. Ghasemi and A. Berenjian, *Nanomaterials*, 2015, **6**, 1.
43 Y. Zhang, L. Jin, Q. Chen, Z. Wu, Y. Dong, L. Han and T. Wang, *Fitoterapia*, 2015, **102**, 7–14.
44 A. Ebrahiminezhad, Y. Barzegar, Y. Ghasemi and A. Berenjian, *Chem. Ind. Chem. Eng. Q.*, 2017, **23**, 31–37.
45 M. A. Hasan, I. M. M. Rahman, M. R. Hossain and F. I. Chowdhury, *Chem. Phys. Impact*, 2025, **10**, 100777.
46 S. Pandit, P. Behera, J. Sahoo and M. De, *ACS Appl. Bio Mater.*, 2019, **2**, 3393–3403.
47 A. Ebrahiminezhad, Y. Barzegar, Y. Ghasemi and A. Berenjian, *Chem. Ind. Chem. Eng. Q.*, 2017, **23**, 31–37.
48 D. M. Aziz, S. J. Mohammed, P. A. Mohammed, S. Al-Zangana, S. B. Aziz, D. S. Muhammad, R. T. Abdulwahid, A. H. A. Darwesh and S. A. Hussein, *Spectrochim. Acta, Part A*, 2025, **325**, 125142.
49 O. K. Hamaamin, H. O. Ghareeb and S. J. Mohammed, *Sci. Rep.*, 2025, **15**, 28891.
50 M. A. Mousa, H. H. Abdelrahman, M. A. Fahmy, D. G. Ebrahim and A. H. E. Moustafa, *Sci. Rep.*, 2023, **13**, 12863.
51 B. De and N. Karak, *RSC Adv.*, 2013, **3**, 8286.
52 B. de Campos Vidal and M. L. S. Mello, *Micron*, 2011, **42**, 283–289.

53 F. Dai, Q. Zhuang, G. Huang, H. Deng and X. Zhang, *ACS Omega*, 2023, **8**, 17064–17076.
54 M. Boumediene, B. Haddad, A. Paolone, M. A. Assenine, D. Villemin, M. Rahmouni and S. Bresson, *J. Mol. Struct.*, 2020, **1220**, 128731.
55 L. Yang, P. W. May, L. Yin, J. A. Smith and K. N. Rosser, *J. Nanopart. Res.*, 2007, **9**, 1181–1185.
56 A. F. Shaikh, M. S. Tamboli, R. H. Patil, A. Bhan, J. D. Ambekar and B. B. Kale, *J. Nanosci. Nanotechnol.*, 2019, **19**, 2339–2345.
57 A. A. Nerantzaki, C. G. Tsiafoulis, P. Charisiadis, V. G. Kontogianni and I. P. Gerothanassis, *Anal. Chim. Acta*, 2011, **688**, 54–60.
58 B. Zghari, P. Doumenq, A. Romane and A. Boukir, *J. Mater. Environ. Sci.*, 2017, **8**, 4496–4509.
59 E. Alexandri, R. Ahmed, H. Siddiqui, M. Choudhary, C. Tsiafoulis and I. Gerothanassis, *Molecules*, 2017, **22**, 1663.
60 S. Upadhyayula, D. Bao, B. Millare, S. S. Sylvia, K. M. M. Habib, K. Ashraf, A. Ferreira, S. Bishop, R. Bonderer, S. Baqai, X. Jing, M. Penchev, M. Ozkan, C. S. Ozkan, R. K. Lake and V. I. Vullev, *J. Phys. Chem. B*, 2011, **115**, 9473–9490.
61 R. Munir, N. Javid, M. Zia-ur-Rehman, M. Zaheer, R. Huma, A. Roohi and M. M. Athar, *Molecules*, 2021, **26**, 4908.
62 B. De and N. Karak, *RSC Adv.*, 2013, **3**, 8286.
63 Z. O. Oyman, W. Ming and R. van der Linde, *Eur. Polym. J.*, 2006, **42**, 1342–1348.
64 Y. Yang, J. Hou, D. Huo, X. Wang, J. Li, G. Xu, M. Bian, Q. He, C. Hou and M. Yang, *Microchim. Acta*, 2019, **186**, 259.
65 M. Vedamalai, A. P. Periasamy, C.-W. Wang, Y.-T. Tseng, L.-C. Ho, C.-C. Shih and H.-T. Chang, *Nanoscale*, 2014, **6**, 13119–13125.
66 K. F. Kayani and C. N. Abdullah, *J. Fluoresc.*, 2024, **35**, 1125–1137.
67 S. J. Mohammed, F. E. Hawaiz, S. B. Aziz and S. H. Al-Jaf, *Opt. Mater.*, 2024, **149**, 115014.
68 A. McEnroe, E. Brunt, N. Mosleh, J. Yu, R. Hailstone and X. Sun, *Talanta Open*, 2023, **7**, 100236.
69 F. R. U. Cortes, E. Falomir, J. Lancis and G. Mínguez-Vega, *Appl. Surf. Sci.*, 2024, **665**, 160326.
70 H. Liu, X. Lv, C. Li, Y. Qian, X. Wang, L. Hu, Y. Wang, W. Lin and H. Wang, *Nanoscale*, 2020, **12**, 10956–10963.
71 H. Yu, Y. Xiang, K. Wu, D. He, X. Chai, L. Xu, Y. Cheng, X. Duan and W. Li, *LWT*, 2024, **208**, 116744.
72 Y.-F. Kang, Y.-H. Li, Y.-W. Fang, Y. Xu, X.-M. Wei and X.-B. Yin, *Sci. Rep.*, 2015, **5**, 11835.
73 K. F. Kayani and C. N. Abdullah, *J. Fluoresc.*, 2024, **35**, 1125–1137.
74 Y. Hao, Y. Song, T. Li, Y. Tuo, M. Tian and F. Chai, *J. Environ. Chem. Eng.*, 2023, **11**, 109863.
75 A.-M. Alam, B.-Y. Park, Z. K. Ghouri, M. Park and H.-Y. Kim, *Green Chem.*, 2015, **17**, 3791–3797.
76 J. V. Rojas, M. Toro-Gonzalez, M. C. Molina-Higgins and C. E. Castano, *Mater. Sci. Eng., B*, 2016, **205**, 28–35.
77 H. Miao, Y. Wang and X. Yang, *Nanoscale*, 2018, **10**, 8139–8145.
78 H. Guo, Y. Lu, Z. Lei, H. Bao, M. Zhang, Z. Wang, C. Guan, B. Tang, Z. Liu and L. Wang, *Nat. Commun.*, 2024, **15**, 4843.
79 B. Murugesan, J. Sonamuthu, N. Pandiyan, B. Pandi, S. Samayanan and S. Mahalingam, *J. Photochem. Photobiol., B*, 2018, **178**, 371–379.
80 M. Vedamalai, A. P. Periasamy, C.-W. Wang, Y.-T. Tseng, L.-C. Ho, C.-C. Shih and H.-T. Chang, *Nanoscale*, 2014, **6**, 13119–13125.
81 K. Jiang, S. Sun, L. Zhang, Y. Wang, C. Cai and H. Lin, *ACS Appl. Mater. Interfaces*, 2015, **7**, 23231–23238.
82 N. Kim, J. Lee, M. Gu and B. Kim, *Carbon Energy*, 2021, **3**, 590–614.
83 M. Tavan, Z. Yousefian, Z. Bakhtiar, M. Rahmandoust and M. H. Mirjalili, *Ind. Crops Prod.*, 2025, **231**, 121207.
84 M. H. Zare and A. Mehrabani-Zeinabad, *Sci. Rep.*, 2022, **12**, 10388.
85 S. El-Sherbiny, F. Morsy, M. Samir and O. A. Fouad, *Appl. Nanosci.*, 2014, **4**, 305–313.
86 S. Hosseinpour, F. Tang, F. Wang, R. A. Livingstone, S. J. Schlegel, T. Ohto, M. Bonn, Y. Nagata and E. H. G. Backus, *J. Phys. Chem. Lett.*, 2017, **8**, 2195–2199.
87 S. Pasieczna-Patkowska, M. Cichy and J. Flieger, *Molecules*, 2025, **30**, 684.
88 L. S. Chougala, M. S. Yatnatti, R. K. Linganagoudar, R. R. Kamble and J. S. Kadadevarmath, *J. Nano- Electron. Phys.*, 2017, **9**, 04005-1–04005-6.
89 N. P. Lata, M. S. Hussain, M. Abdulla-Al-Mamun, T. U. Rashid and S. M. Shamsuddin, *Heliyon*, 2024, **10**, e29255.
90 E. A. Al-Oubidy and F. J. Kadhim, *Opt. Quantum Electron.*, 2019, **51**, 23.
91 B.-C. Bui, N.-N. Vu, H.-E. Nemamcha, H. T. Nguyen, V.-A. Nguyen and P. Nguyen-Tri, *J. Water Process Eng.*, 2025, **70**, 106904.
92 S. S. Ghumro, B. Lal and T. Pirzada, *ACS Omega*, 2022, **7**, 4333–4341.
93 A. I. Kontos, I. M. Arabatzis, D. S. Tsoukleris, A. G. Kontos, M. C. Bernard, D. E. Petrakis and P. Falaras, *Catal. Today*, 2005, **101**, 275–281.
94 R. Liu, H. Li, L. Duan, H. Shen, Y. Zhang and X. Zhao, *Ceram. Int.*, 2017, **43**, 8648–8654.
95 R. M. S. Sendão, M. Algarra, J. Lázaro-Martínez, A. T. S. C. Brandão, A. Gil, C. Pereira, J. C. G. Esteves da Silva and L. Pinto da Silva, *Colloids Surf., A*, 2025, **713**, 136475.
96 X. Zhang, S. Lu, D. He, M. Chai, Z. Wu, X. Yao and Y. Yang, *Trans. Nonferrous Met. Soc. China*, 2023, **33**, 2395–2405.
97 H. Huang, H. Ouyang, T. Han, H. Wang and X. Zheng, *RSC Adv.*, 2019, **9**, 3532–3541.
98 X. Zeng, Z. Wang, N. Meng, D. T. McCarthy, A. Deletic, J. Pan and X. Zhang, *Appl. Catal., B*, 2017, **202**, 33–41.
99 A. Mozdbar, A. Nouralishahi, S. Fatemi and F. S. Talatori, *J. Water Process Eng.*, 2023, **51**, 103465.
100 J. Chen, J. Shu, Z. Anqi, H. Juyuan, Z. Yan and J. Chen, *Diamond Relat. Mater.*, 2016, **70**, 137–144.
101 J. Tauc, R. Grigorovici and A. Vancu, *Phys. Status Solidi B*, 1966, **15**, 627–637.

102 M. M. A. El Raheem, M. M. Wakkad, H. A. Mohamed, N. A. Hamed and H. F. Mohamed, *J. Mater. Sci.:Mater. Eng.*, 2025, **20**, 95.
103 P. Kubelka and F. Munk, *Z. Tech. Phys.*, 1931, **12**, 193.
104 R. López and R. Gómez, *J. Sol-Gel Sci. Technol.*, 2012, **61**, 1–7.
105 H. F. Haneef, A. M. Zeidell and O. D. Jurchescu, *J. Mater. Chem. C*, 2020, **8**, 759–787.
106 K. Jarzynska, K. Ciura, X. J. Gao, A. Mikolajczyk, X. Gao and T. Puzyn, *Nano Today*, 2025, **64**, 102783.
107 D. A. Kader, S. A. Abdalla, S. J. Mohammed, D. M. Aziz, D. D. Ghafoor, T. M. Abdullah, N. N. M. Agha, F. S. Mustafa and S. A. Hassan, *J. Photochem. Photobiol., A*, 2025, **462**, 116253.
108 S. Albukhaty, L. Al-Bayati, H. Al-Karagoly and S. Al-Musawi, *Anim. Biotechnol.*, 2022, **33**, 864–870.
109 N. Daneshvar, D. Salari and A. R. Khataee, *J. Photochem. Photobiol., A*, 2003, **157**, 111–116.
110 I. K. Konstantinou and T. A. Albanis, *Appl. Catal., B*, 2004, **49**, 1–14.
111 A. Rafiq, M. Ikram, S. Ali, F. Niaz, M. Khan, Q. Khan and M. Maqbool, *J. Ind. Eng. Chem.*, 2021, **97**, 111–128.
112 M. B. K. Suhan, M. R. Al-Mamun, N. Farzana, S. M. Aishee, M. S. Islam, H. M. Marwani, M. M. Hasan, A. M. Asiri, M. M. Rahman, A. Islam and M. R. Awual, *Nano-Struct. Nano-Objects*, 2023, **36**, 101050.
113 N. Ramesh, C. W. Lai, M. R. Bin Johan, S. M. Mousavi, I. A. Badruddin, A. Kumar, G. Sharma and F. Gapsari, *Heliyon*, 2024, **10**, e40998.
114 N. Kim, J. Lee, M. Gu and B. Kim, *Carbon Energy*, 2021, **3**, 590–614.
115 F. Zhao, Y. Rong, J. Wan, Z. Hu, Z. Peng and B. Wang, *Catal. Today*, 2018, **315**, 162–170.
116 C. Guillard, H. Lachheb, A. Houas, M. Ksibi, E. Elaloui and J.-M. Herrmann, *J. Photochem. Photobiol., A*, 2003, **158**, 27–36.
117 K. Chen, W. Dong, Y. Huang, F. Wang, J. L. Zhou and W. Li, *J. Environ. Chem. Eng.*, 2025, **13**, 117529.
118 I. K. Konstantinou and T. A. Albanis, *Appl. Catal., B*, 2004, **49**, 1–14.
119 J. Trakulmututa, C. Chuaicham, A. Srikhaow and K. Sasaki, *Sustainable Mater. Technol.*, 2024, **42**, e01129.
120 Y. Lin, D. Li, J. Hu, G. Xiao, J. Wang, W. Li and X. Fu, *J. Phys. Chem. C*, 2012, **116**, 5764–5772.
121 M. Umair, C. M. Pecoraro, F. Di Franco, M. Santamaria, L. Palmisano, V. Loddo and M. Bellardita, *Sustainable Mater. Technol.*, 2025, **43**, e01188.
122 N. Ramesh, C. W. Lai, M. R. Bin Johan, S. M. Mousavi, I. A. Badruddin, A. Kumar, G. Sharma and F. Gapsari, *Heliyon*, 2024, **10**, e40998.
123 E. Palma Soto, C. A. Rodriguez Gonzalez, P. A. Luque Morales, H. Reyes Blas and A. Carrillo Castillo, *Catalysts*, 2024, **14**, 589.
124 G. E. Quintanilla-Villanueva, A. Sicardi-Segade, D. Luna-Moreno, R. E. Núñez-Salas, J. F. Villarreal-Chiu and M. M. Rodríguez-Delgado, *Catalysts*, 2025, **15**, 84.